Research Article

Farhan Ali, Aurang Zaib, Syed Sohaib Zafar, Umair Khan, Muhammad Faizan Ahmed*, Samia Elattar, and Najiyah Safwa Khashi'ie

Use of artificial neural network for optimization of irreversibility analysis in radiative Cross nanofluid flow past an inclined surface with convective boundary conditions

https://doi.org/10.1515/htmp-2025-0080
received November 05, 2024; accepted May 09, 2025

Abstract: This study uses an artificial intelligence neural network to estimate the solution for a Cross-nanofluid containing gyrotactic microorganisms on an inclined surface. Furthermore, the concept of minimizing entropy has been taken into account. The energy and concentration equations take into account the importance of thermal radiation, convective flow, heat source/sink, and chemical processes. By applying an appropriate similarity transformation, the modeled equations are converted into ordinary differential equations. The equations are solved numerically using an artificial neural network (ANN) that employs the Levenberg–Marquardt approach. To evaluate the correctness of the proposed model, the results of training, testing, and validation are analyzed using the performance charts, error histograms, transition state analysis, comparisons between bvp4c and ANN, and regression plots. In addition, a bigger estimation of the radiative variable and the Biot number results in a rise in the temperature of the fluid. Conversely, greater values of the Prandtl number lead to a diminution in the temperature. Growing the Weissenberg parameter enhances the velocity and decreases both the Bejan number and entropy generation. To showcase the accuracy of the numerical approach that has been applied, a comparison table is provided, which displays a remarkable level of agreement when compared to previously published data.

Keywords: Cross fluid, bio-convective flow, nanofluid, entropy generation, ANN, Levenberg–Marquardt approach, thermal radiation

*** Corresponding author: Muhammad Faizan Ahmed**, Department of Mathematical Sciences, Federal Urdu University of Arts, Sciences & Technology, Gulshan-e-Iqbal, Karachi, 75300, Pakistan, e-mail: mfaizanahmed@fuuast.edu.pk
Farhan Ali: Department of Mathematical Sciences, Federal Urdu University of Arts, Sciences & Technology, Gulshan-e-Iqbal, Karachi, 75300, Pakistan, e-mail: farhanali.ali15@gmail.com
Aurang Zaib: Department of Mathematical Sciences, Federal Urdu University of Arts, Sciences & Technology, Gulshan-e-Iqbal, Karachi, 75300, Pakistan, e-mail: aurangzaib@fuuast.edu.pk
Syed Sohaib Zafar: Department of Mathematics and Sciences, Sir Syed University of Engineering and Technology, Gulshan-e-Iqbal, Karachi, 75300, Pakistan, e-mail: sohaib.zafar@ssuet.edu.pk
Umair Khan: Department of Mathematics, Saveetha School of Engineering, Saveetha Institute of Medical and Technical Sciences, Saveetha University, Chennai, 602105, Tamil Nadu, India; Department of Mathematics, Faculty of Science, Sakarya University, Serdivan/Sakarya, 54050, Turkey, e-mail: umairkhan@sakarya.edu.tr
Samia Elattar: Department of Industrial and Systems Engineering, College of Engineering, Princess Nourah bint Abdulrahman University, P.O. Box 84428, Riyadh 11671, Saudi Arabia, e-mail: SAElattar@pnu.edu.sa
Najiyah Safwa Khashi'ie: Fakulti Teknologi dan Kejuruteraan Mekanikal, Universiti Teknikal Malaysia Melaka, Hang Tuah Jaya, 76100, Durian Tunggal, Melaka, Malaysia, e-mail: najiyah@utem.edu.my

Abbreviations

ANN	artificial neural network
AINN	artificial intelligence neural network
MSE	mean squared error
MLP	multi-layer perceptron
FFBP	feed-forward back-propagation

1 Introduction

The area of non-Newtonian fluid flows has gained considerable attention due to its substantial physiological, engineering, and biological importance. In engineering, the impacts of thermal and convective transport in non-Newtonian fluids, such as slurries, industrial equipment thermal design, food, and so on, are very relevant. The research involving non-

Newtonian fluids remains relevant and intriguing as the theory of Navier–Stokes equations is inadequate for several complicated rheological fluids. Various non-Newtonian fluid models, such as Maxwell, Eyring–Powell, Casson, and Williamson models, have been created to account for the diverse properties of fluids, as no single model can encompass all of them. The Cross-fluid model [1] was planned by Cross to depict the properties of fluids with larger and lower shear rates. Haghighi et al. [2] explored the velocity of Cross fluid in a blood flow through a cylindrical tube subject to a non-symmetric stenosis artery. Nazeer [3] talked about the thermal transport through Cross fluid using a rate of heat generation and radiative flow. The multiple slip effects on the Cross fluid due to inclined magnetic effect in the presence of activation energy and the radiative effect were discovered by Sabir et al. [4]. The chemical reaction with Cross flow of orthogonal bonding hydrogen and Lorentz dipole has been done by Yao et al. [5]. Khan et al. [6] labeled the impact of activation energy and radiative flow with the thermophoretic effect for the Cross fluid near the stagnant flow. Shah et al. [7] elucidated the Cross nanomaterial by considering (Fe_3O_4) nanoparticles in the blood through the rate of homogeneous–heterogeneous. Ali et al. [8] studied the first-order chemical reactions involving nanofluids induced by a Cross fluid via a rotating cylinder in the presence of magnetic and heat generation effects concerning the time-dependent flow. Salahuddin et al. [9] studied the role of activation energy on the Cross fluid under double stratification over a stretched sheet with MHD and heat generation. Shi et al. [10] inspected the time-dependent flow of chemical reactive of bioconvection in a Cross nanofluid with thermal radiative due to a stretched plate. Shoaib et al. [11] utilized the Levenberg–Marquardt algorithm along with back-propagated artificial neural networks (ANNs) to conduct an intelligence-based numerical inquiry. The focus of their analysis was the nonlinear radiative stagnation point flow of a Cross-nanofluid system across a stretched surface.

Bioconvection is employed in multitude applications within biological and biotechnological processes. The word “bioconvective” refers to the collective motion of liquid caused by a density differential resulting from the coordinated swim of motile microorganisms. Through directed movement, the bacteria that are capable of moving on their own enhance with their population density. By introducing an ordinary liquid, bioconvection is triggered. The role of bioconvection with nanoliquid convection is linked to the existence of more concentrated microorganisms that gather on the less dense surface of the water. As denser microorganisms descend, the presence of upward-swimming microorganisms in the water replenishes the nutrients, determining the process of bioconvection in the system. The mechanism is a phenomenon that occurs at the mesoscale, where the motion of motile things causes a macroscopic movement. The natural convection boundary layer flows across a flat surface in a nanoliquid that contains gyrotactic microorganisms was conducted by Aziz et al. [12]. Tham et al. [13] computed an analysis of mixed convective boundary layer flow around a solid surface that was saturated. Ibrahim [14] explored the time-dependent flow of a viscous fluid caused by a revolving disk that can stretch. Chu et al. [15] investigated the properties of nonlinear thermal radiative with heat generation in a Maxwell nanoliquid containing gyrotactic microorganisms using a bidirectional moving sheet. The heat transfers for Casson nanofluids containing gyrotactic bacteria, by considering the effects of MHD and thermal radiation on a stretched surface are observed by Islam et al. [16]. Khan et al. [17] scrutinized the 2D flow by using motile microbes incorporated Oldroyd-B nanoparticles with the Cattaneo–Christov effect in a porous channel. Nadeem et al. [18] inspected the transport of nanomaterial at a stagnation point using a micropolar fluid past a stretchable sheet. Ferdows et al. [19] examined the movement of microorganisms containing nanoliquid due to a cylinder. Sajid et al. [20] conducted a study on a nanoliquid that exhibits double-diffuse tangent hyperbolic behavior. Usman et al. [21] scrutinized the analysis of nonlinear thermal radiative for the energy with the rate of mass in the microorganism of non-Newtonian bio-nanofluid past a Riga sheet. Hussain et al. [22] explored the process of optimizing entropy in a microorganism, chemically reactive flow of micropolar nanomaterials. This flow also involved activation energy and gyrotactic microorganisms. Olkha and Choudhary [23] examined the energy transmission with entropy formation in a viscous nanofluid flow containing microorganisms past an inclined exponential stretchable porous surface. In their study, the fluid dynamics are analyzed as it passes through a permeable substance. Ali et al. [24] considered the entropy on the Darcian–Forchheimer flow of Cross fluid comprising microorganism and nanoparticles passing a flexible cylinder with velocity slip, Arrhenius kinetics, and predictions of chemical reactions. They discovered that the Sherwood number is positively influenced by activation energy, but it decreases dramatically as the chemical reaction advances. Bilal et al. [25] evaluated the magneto-bioconvection properties through a bidirectional flow of Cross fluid past a horizontally stretched sheet with ternary stratification effects. They discovered that the addition of microbes to nanofluids improves the thermal properties of the fluid and promotes flow stability.

Nanofluid refers to a category of nanotechnology that utilizes heat transfer fluids. Nanofluid is created by effectively mixing and distributing nanoparticles within a conventional fluid, resulting in a fluid with a size of

approximately 100 nm. The word "nanofluid" was first presented by Choi and Eastman [26], who used it to describe a new form of nanotechnology that involves the manipulation of thermal characteristics. The goal of nanofluid is to obtain maximum thermal efficiency with the lowest possible concentration. Nanofluid optimizes heat conductivity. Nanoparticles are synthesized consisting of metallic elements, carbon nanotubes, carbides, and other substances. Nanofluids, consisting of tiny particles resembling fog or fine dust, are being employed in solar energy systems and heat exchangers. Automotive heaters and electronic chips, among other things. The circulation of nanofluid through an artery with a combination of a narrowed passage and walls that allow the passage of substances is stated by Ellahi et al. [27]. Rashidi et al. [28] studied the formation of entropy in the presence of magnetic blood flow of nanofluid caused by peristaltic waves. Chahregh and Dinarvand [29] published their research on the flow of TiO_2–Ag/blood hybrid nanofluid via an artery, focusing on its potential applications in medication delivery. They also discussed the transportation and distribution of substances in the respiratory system. Manjunatha et al. [30] investigated the flow of nonlinear thermal radiative through heterogeneous/homogenous nanomaterial past a stretched sheet. Sheikholeslami [31] employed an innovative computer-based method to examine the magneto flow of Al_2O_3 nanofluid in a permeable porous medium. Ayub et al. [32] examined the complex dynamics of MHD stagnant flow of nanofluid past a cylinder. They investigated the impacts of changing thermal conductivity, Lorentz's force, and cylindrical coordinates on the unsteady flow. Ramesh et al. [33] showed a comprehensive analysis of the neural network model on the hybrid nanofluid with activation energy. They studied the interaction between nanoparticles, gyrotactic microorganisms, and the bioconvection process and investigated their impact on fluid dynamics. Alharbi et al. [34] described the Hall current in viscous nanofluid with a heated convective sheet. Vinothkumar et al. [35] probed the nanoparticles of heat and mass transport on the magneto flow past a stretching sheet. Tanuja et al. [36] discovered the effect of a trihybrid nanofluid with porous substance by utilizing the machine learning approach.

When analyzing the flow and heat transfer methods in thermodynamic processes, it is critical to improve the effectiveness of thermal systems to minimize heat loss. This reduction in heat loss is quantitatively measured as entropy generation. Bejan [37] and Bejan and Kestin [37,38] pioneered the calculation of the ratio of entropy analysis during the fluid procedure. Qing et al. [39] computed the magneto-nanofluid for the viscoelastic Casson fluid subject to the entropy analysis. Sithole et al. [40] examined chemical interactions occurring on a secondary level and evaluated the performance of a nanofluid on a heated stretchable surface under nonlinear thermal radiation. Shit and Mukherjee [41] conducted a study on the utilization of Maxwell nanofluid in a system consisting of two squeezing plates while taking into account the impact of thermal radiation. Abbas et al. [42] performed the irreversibility analysis on Cross flow comprising nanofluid under viscous dissipation past a vertical stretching sheet. Siddiqui et al. [43] inspected the mathematical analysis of the entropy generation by considering Cu and Al_2O_3 hybrid nanofluid over the stretched cylinder with homogenous/heterogeneous reaction. Recently, Tlili et al. [44] described the influence of viscous dissipation on the Darcy–Forchheimer flow of Williamson nanofluid subject to the chemical reaction and second law analysis.

AINNS were also very important in the modeling of the mass and heat transfer problems. Unlike the standard analytical and numerical methods, they offer a useful alternative for figuring out how heat and mass move. It works well for both complicated and nonlinear issues. Researchers often use it instead of traditional mathematical methods because it can learn quickly and accurately guess what will happen. Shafiq et al. [45] studied the solar radiation and heat generation absorption induced by the microorganism using the Levenberg–Marquardt method and a back-propagated neural network. Their research found that hyperbolic tangent fluids have much faster heat transfer rates than Newtonian fluids. Akbar et al. [46] explained the significance of neural networks for the Levenberg–Marquardt technique of hybrid nanofluid induced by second law analysis. Chandra and Das [47] examined the use of a hybrid machine-learning algorithm to analyze the movement of magneto-bio-nanofluid with gyrotactic microorganisms over a vertically inclined stretching surface. Akbar et al. [48] explored the convective flow of the Levenberg–Marquardt technique in the hybrid nanofluid considering a neural machine network. Shah et al. [49] discovered the irreversibility analysis of tri-hybrid tangent hyperbolic nanofluid considering the Levenberg–Marquardt technique. Alghamdi et al. [50] carried out the numerical study of the neural network of the Eyring–Powell nanomaterial past stretchable cylinder. Srinivasacharya and Kumar [51] utilized neural network analysis to investigate the bioconvection flow of Casson fluid over a vertically expanding sheet. Alghamdi et al. [52] scrutinized the micropolar flow of mixed convective nanofluid for the dual stratified condition induce by neural computing network.

This study utilizes an ANN model to calculate radiative heat transfer and entropy in a 2D bioconvection flow of Cross-nanomaterial past an inclined sheet. This particular

topic has not been extensively explored in the existing literature. The objective of our research is to evaluate the suitability of the Levenberg–Marquardt backpropagation neural network for evaluating the flow of Cross nanofluid under the subject to radiation and microorganisms. We aim to use the proven effectiveness of ANN models in tackling nonlinear issues. We systematically examine these intricate phenomena and provide numerical findings that are compared to those obtained by the ANN methodology. To facilitate engineering predictions on inclined surfaces, we develop a neural network model that is extensively assessed in terms of regression analysis, zero error, and mean square error.

2 Mathematical formulation

A study is conducted to assess the flow of Cross nanoliquid past a tilt sheet. The inclination angle, denoted by ω, represents the angle formed between the orientation of the plate and the vertical direction. Assuming that the fluid flow is not compressible, a Cartesian coordinate system is employed. The coordinate axes are formed by orienting the x-axis in parallel with the flow direction and positioning the y-axis in an upward direction, as seen in Figure 1. The presence of thermal radiation, a source or sink of heat, and chemical processes in the fluid flow is taken into account. The Buongiorno model is employed to examine the characteristics of the nanomaterial, such as thermophoresis and Brownian motion. In this context, T_f denotes the convective temperature of the liquid, whereas C_w and Π_w represent the concentration and gyrotactic bacteria at the wall, respectively. The variables representing temperature, concentration, and microbe levels far away from the surface are denoted as T_∞, C_∞, and Π_∞, respectively. The constitutive expression for the Cross-fluid model can be found in [11,24,32,42]

$$\left.\begin{aligned} \tau &= \mu(\dot{\beta})B_1 - \mathrm{PI}, \\ \mu(\dot{\beta}) &= \frac{\mu_\infty(1 + (\Gamma\dot{\beta})^n) + \mu_0 - \mu_\infty}{1 + (\Gamma\dot{\beta})^n}. \end{aligned}\right\} \tag{1}$$

Here, n is the index power law, $B_1 = (\text{grad } \boldsymbol{V})^T + (\text{grad } \boldsymbol{V})$ denoted the Erickson Rivlin tensor, I is the identity tensor, P is the pressure, $\dot{\beta} = \sqrt{\frac{1}{2}\sum_i\sum_j \dot{\beta}_{ij}\dot{\beta}_{ji}} = \sqrt{\frac{1}{2}\text{tr}(B_1^2)}$ is represented by shear stress, μ stands for the viscosity, μ_0 is

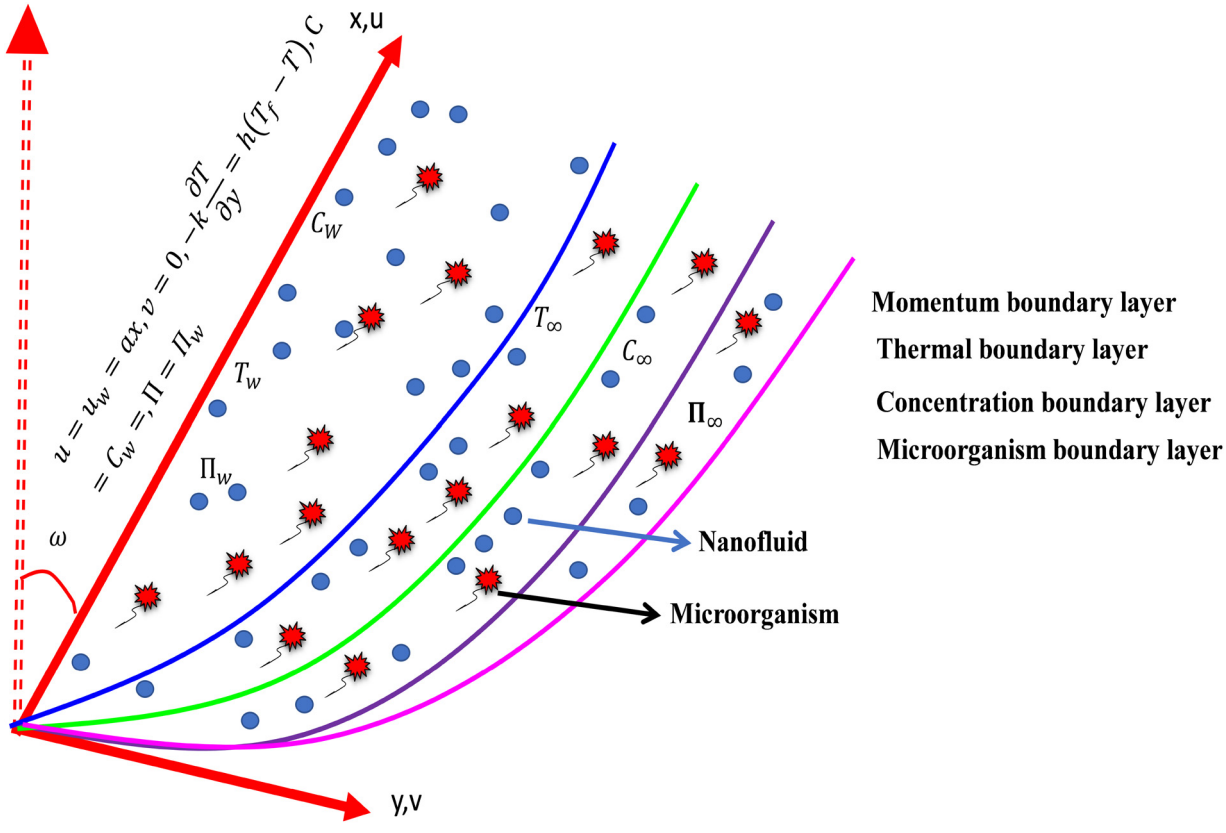

Figure 1: Geometry of the flow problem.

the zero shear rates, μ_∞ is the infinite shear rate, and Γ is the material time constant. The Cross viscosity model in terms of shear stress for the current investigation can be written as

$$\dot{\beta} = \left[\left(\frac{\partial u}{\partial y} + \frac{\partial v}{\partial y}\right)^2 + 4\left(\frac{\partial u}{\partial x}\right)^2\right]^{1/2}. \tag{2}$$

Momentum, thermal layer, concentration, and microorganism for 2D flow are expressed as

$$\begin{aligned} &V = [u(x,y), v(x,y), 0], \quad T = T(x,y), \quad C = C(x,y), \\ &\Pi = \Pi(x,y). \end{aligned} \tag{3}$$

The constitutive equations are formulated as follows, taking into account the constraints discussed before [11,22,24,32,42].

The following assumptions have been made in this analysis:

- The inclined angel ω is applied to the flow system.
- The heat source/sink and thermal radiations are taken into account to regulate the thermal effects on the fluid flow.
- The Buongiorno model is applied to the flow system to capture the thermophoretic and Brownian motion characteristics resulting from the nanofluid flow.
- The flow system is also subjected to a collective influence of chemical reaction effects.
- The convective boundary conditions are employed to optimize the thermal transport of the Cross nanofluid.

$$\frac{\partial u}{\partial x} + \frac{\partial v}{\partial y} = 0, \tag{4}$$

$$\left.\begin{aligned} &u\frac{\partial u}{\partial x} + v\frac{\partial u}{\partial y} \\ &= \nu_f \frac{\partial^2 u}{\partial y^2}\left[\frac{1}{1 + \left(\Gamma\frac{\partial u}{\partial y}\right)^n}\right] + \frac{1}{\rho_f}((1 - C_\infty)g\rho_f\gamma_1(T - T_\infty) \\ &- (\rho_p - \rho_f)g(C - C_\infty) - \gamma_2(\rho_m - \rho_f)g(\Pi - \Pi_\infty))\cos\omega, \end{aligned}\right\} \tag{5}$$

$$\begin{aligned} &u\frac{\partial T}{\partial x} + v\frac{\partial T}{\partial y} - \left(\alpha_f + \frac{16\sigma^* T_\infty^3}{3k(\rho C_p)_f}\right)\frac{\partial^2 T}{\partial y^2} \\ &= \tau\left[D_B\frac{\partial C}{\partial y}\frac{\partial T}{\partial y} + \frac{D_T}{T_\infty}\left(\frac{\partial T}{\partial y}\right)^2\right] + \frac{Q_0}{(\rho C_p)_f}(T - T_\infty), \end{aligned} \tag{6}$$

$$u\frac{\partial C}{\partial x} + v\frac{\partial C}{\partial y} = D_B\frac{\partial^2 C}{\partial y^2} + \frac{D_T}{T_\infty}\frac{\partial^2 T}{\partial y^2} - K_0(C - C_\infty), \tag{7}$$

$$u\frac{\partial \Pi}{\partial x} + v\frac{\partial \Pi}{\partial y} + \frac{bW_c}{C_w - C_\infty}\left(\frac{\partial}{\partial y}\left(\Pi\frac{\partial C}{\partial y}\right)\right) = D_m\frac{\partial^2 \Pi}{\partial y^2}. \tag{8}$$

The boundary constraints are applied as follows:

$$\left.\begin{aligned} &u = u_w = ax, \ v = 0, \ -k\frac{\partial T}{\partial y} = h(T_f - T), \ C = C_w, \\ &\Pi = \Pi_w \ \text{ at } \ y = 0 \\ &u \to 0, \ v \to 0, \ T \to T_\infty, \ C \to C_\infty, \ \Pi \to \Pi_\infty \ \text{ as } \ y \to \infty. \end{aligned}\right\} \tag{9}$$

The velocity can be decomposed into its components along the x-axis and y-axis, which is denoted as u and v, respectively. ρ_f exhibits the fluid density, ρ_f is described as the density of nanoparticles, ρ_m is denoted by the density of microorganisms, $(\rho C_p)_f$ is denoted by heat specific capacity of fluid, Q_0 is the coefficient of heat source/sink, T is the temperature of the fluid, α_f is the thermal diffusivity, D_m is described by microorganisms, b is the chemotaxis constant, W_c is the cell swimming speed, D_B is defined as diffusive thermophoretic, σ^* presents the Stefan–Boltzmann constant, τ is explained as the heat capacity ratio of nanofluid, K_0 defines chemical reactions, υ is defined as viscosity kinematics, γ_1 and γ_2 presents the volumetric thermal expansion coefficient and the average volume of microorganisms respectively, and g stands for gravity. Using the following appropriate similarity transformation:

$$\left.\begin{aligned} &u = axF'(\xi), \ v = -\sqrt{a\nu}\,F(\xi), \ \xi = y\sqrt{\frac{a}{\nu}}, \\ &\vartheta(\xi) = \frac{T - T_\infty}{T_f - T_\infty}, \ \Phi(\xi) = \frac{C - C_\infty}{C_w - C_\infty}, \ \Upsilon(\xi) = \frac{\Pi - \Pi_\infty}{\Pi_w - \Pi_\infty}, \end{aligned}\right\} \tag{10}$$

Subsequently, by implementing the aforementioned similarity transformation to equations (4)–(8), the resulting equations are nonlinear and non-dimensional ordinary differential equations (ODEs) stated as below:

$$\left.\begin{aligned} &[(1 + (1 - n)(\mathrm{We}\ F'')^n)]F''' \\ &\quad + [FF'' - F'^2]\{1 + (\mathrm{We}\ F'')^n\}^2 \\ &+ \cos\ \omega\lambda(\vartheta - \gamma_c\,\Phi - \gamma_m\Upsilon)\{1 + (\mathrm{We}\ F'')^n\}^2 = 0, \end{aligned}\right\} \tag{11}$$

$$\begin{aligned} &\vartheta''\left(1 + \frac{4}{3}\mathrm{Rd}\right) + \mathrm{Pr}\ \delta\vartheta + \mathrm{Pr}\ F\vartheta' + \mathrm{Pr}\ \mathrm{Nb}\ \vartheta'\Phi' \\ &\quad + \mathrm{Pr}\ \mathrm{Nt}\ \vartheta'^2 = 0, \end{aligned} \tag{12}$$

$$\Phi'' + \mathrm{Sc}\ F\Phi' + \frac{\mathrm{Nt}}{\mathrm{Nb}}\vartheta'' - \mathrm{Sc}\ \mathrm{Kr}\ \ \Phi = 0, \tag{13}$$

$$\Upsilon'' + \mathrm{Lb}\ F\Upsilon' - \mathrm{Pe}[\Upsilon'\Phi' + \Phi''(\Upsilon + \Omega) = 0]. \tag{14}$$

The symbol ξ' represents the derivative with regard to ξ, and the dimensionless physical variables are explained below:

$\mathrm{We} = \Gamma a\ \ \mathrm{Re}^{1/2}$ is the Weissenberg number, $\mathrm{Sc} = \frac{\nu}{D_B}$ is the Schmidt number, $\lambda = \frac{(1 - C_\infty)(T_f - T_\infty)\lambda_1 g}{cu_w}$ is a mixed convec-

tive parameter, $\delta = \frac{Q_0}{a(\rho C_p)_f}$ is the heat source/sink parameter, $\gamma_c = \frac{(\rho_p - \rho_f)(C_w - C_\infty)}{\lambda_1(1 - C_\infty)(T_f - T_\infty)\rho_f}$ is the buoyancy parameter, $\mathrm{Lb} = \frac{\nu}{D_m}$ is the bioconvection Lewis number, $\gamma_m = \frac{\lambda_2(\rho_m - \rho_f)(\Pi_w - \Pi_\infty)}{\lambda_1(1 - C_\infty)(T_f - T_\infty)\rho_f}$ is the bioconvection Rayleigh number, $\mathrm{Pr} = \frac{\nu}{\alpha_f}$ is the Prandtl number, $\mathrm{Nb} = \frac{\tau D_B(C_w - C_\infty)}{\nu}$ is the Brownian motion, $\mathrm{Rd} = \frac{4\sigma^* T_\infty^3}{k^* k}$ is the thermal radiation, $\Omega = \frac{\Pi_\infty}{\Pi_w - \Pi_\infty}$ is the microorganism difference parameter, $\mathrm{Pe} = \frac{bWc}{D_m}$ is the Peclet number, $\mathrm{Nt} = \frac{\tau D_T(T_f - T_\infty)}{\nu T_\infty}$ is the thermophoretic diffusion, $\mathrm{Kr} = \frac{K_0}{a}$ is the chemical reaction parameter, and $\mathrm{Bi} = \frac{h_f}{k}\sqrt{\frac{\nu}{a}}$ is the Biot number.

The boundary conditions are

$$\left.\begin{aligned} &F(0) = 0,\ F'(0) = 1,\ \vartheta'(0) = -\mathrm{Bi}(1 - \vartheta(0)),\\ &\Phi(0) = 1,\ \ \mathrm{Y}(0) = 1,\\ &F'(\infty) \to 0,\ \ \vartheta(\infty) \to 0,\ \ \Phi(\infty) \to 0,\ \ \mathrm{Y}(\infty) \to 0. \end{aligned}\right\} \tag{15}$$

The engineering-relevant physical quantities are [11,32,39]

$$\left.\begin{aligned} C_f &= \frac{\tau_w}{\rho_f u_w^2},\\ \mathrm{Nu} &= \frac{x q_w}{k_1(T_f - T_\infty)},\\ \mathrm{Sh} &= \frac{x q_m}{D_B(C_w - C_\infty)},\\ \mathrm{Nh} &= \frac{x q_n}{D_m(\Pi_w - \Pi_\infty)}. \end{aligned}\right\} \tag{16}$$

τ_w, q_w, q_m, and q_n are explained as

$$\left.\begin{aligned} \tau_w &= \mu_o \frac{\partial u}{\partial y}\left(\frac{1}{1 + \left(\Gamma \frac{\partial u}{\partial y}\right)^n}\right)\Bigg|_{y=0},\\ q_w &= -k_1\left(1 + \frac{16\sigma^* T_\infty^3}{3kk_1}\right)\frac{\partial T}{\partial y}\Bigg|_{y=0},\\ q_m &= -D_B \frac{\partial C}{\partial y}\Bigg|_{y=0},\\ q_n &= -D_m \frac{\partial \Pi}{\partial y}\Bigg|_{y=0}. \end{aligned}\right\} \tag{17}$$

Utilizing equations (16) and (17), we obtain

$$\left.\begin{aligned} \mathrm{Cf}\ \mathrm{Re}^{0.5} &= \left[\frac{1}{1 + (\mathrm{We}\ F''(0))^n}\right]F''(0),\\ \mathrm{Nu}\ \mathrm{Re}^{-0.5} &= -\vartheta'(0)\left[1 + \frac{4}{3}\mathrm{Rd}\right],\\ \mathrm{Sh}\ \mathrm{Re}^{-0.5} &= -\Phi'(0),\\ \mathrm{Nh}\ \mathrm{Re}^{-0.5} &= -\mathrm{Y}(0). \end{aligned}\right\} \tag{18}$$

3 Entropy analysis

The rate of entropy production $\mathrm{Ns}(\xi)$ for the Cross fluid through radiative and diffusion effects can be written as [22,24,42]

$$\left.\begin{aligned} \mathrm{Es}(\xi) = {} & \frac{\mu}{T_\infty}\left(\frac{\partial u}{\partial y}\right)^2\left\{\frac{1}{1 + \left(\Gamma \frac{\partial u}{\partial y}\right)^n}\right\} + \frac{k_1}{T_\infty^2}\left(1 + \frac{16\sigma^* T_\infty^3}{3kk_1}\left(\frac{\partial T}{\partial y}\right)^2\right)\\ & + \frac{\mathrm{RD}_m}{C_\infty}\left(\frac{\partial C}{\partial y}\right)^2 + \frac{\mathrm{RD}_m}{T_\infty}\left(\frac{\partial T}{\partial y}\right)\left(\frac{\partial C}{\partial y}\right) + \frac{\mathrm{RD}_m}{\Pi_\infty}\left(\frac{\partial \Pi}{\partial y}\right)^2\\ & + \frac{\mathrm{RD}_m}{T_\infty}\left(\frac{\partial \Pi}{\partial y}\right)\left(\frac{\partial T}{\partial y}\right). \end{aligned}\right\} \tag{19}$$

The non-dimensionless entropy analysis is explained as

$$\left.\begin{aligned} \mathrm{Ns}(\xi) = {} & \beta_2\left(1 + \frac{4}{3}\mathrm{Rd}\right)\vartheta'^2 + \mathrm{Br}\left[\frac{1}{(1 + (\mathrm{We}\ F'')^n)}\right](F'')^2\\ & + P_1\frac{\beta_1}{\beta_2}\Phi'^2 + P_1\Phi'\vartheta' + P_2\frac{L}{\beta_2}\Upsilon'^2 + P_2\Upsilon'\vartheta' \end{aligned}\right\} \tag{20}$$

The Bejan number (Be) describes as

$$\mathrm{Be}(\xi) = \frac{\beta_2\left(1 + \frac{4}{3}\mathrm{Rd}\right)\vartheta'^2 + P_1\frac{\beta_1}{\beta_2}\Phi'^2 + P_1\Phi'\vartheta' + P_2\frac{L}{\beta_2}\Upsilon'^2 + P_2\Upsilon'\vartheta'}{\beta_2\left(1 + \frac{4}{3}\mathrm{Rd}\right)\vartheta'^2 + \mathrm{Br}\left[\frac{1}{(1 + (\mathrm{We}\ F'')^n)}\right](F'')^2 + P_1\frac{\beta_1}{\beta_2}\Phi'^2 + P_1\Phi'\vartheta' + P_2\frac{L}{\beta_2}\Upsilon'^2 + P_2\Upsilon'\vartheta'}. \tag{21}$$

4 Numerical procedure

The highly coupled differential equations with non-dimensional boundaries, as outlined in equations (11)–(14), have been solved using the Lobatto IIIa finite difference shooting method bvp4c in the simulation software MATLAB. This method has been employed to obtain numerical outcomes for momentum, temperature, concentration, and microorganism density. The system of equations can be expressed as

$$\left.\begin{aligned} &F = M_1,\ \frac{\mathrm{d}F}{\mathrm{d}\xi} = M_2,\ \frac{\mathrm{d}^2F}{\mathrm{d}\xi^2} = M_3,\\ &\frac{\mathrm{d}^3F}{\mathrm{d}\xi^3} = \frac{\mathrm{d}M_3}{\mathrm{d}\xi}\\ &\vartheta = M_4,\ \frac{\mathrm{d}\vartheta}{\mathrm{d}\xi} = M_5,\ \vartheta'' = \frac{\mathrm{d}M_5}{\mathrm{d}\xi}\\ &\Phi{=}M_6,\ \Phi' = M_7,\ \Phi'' = \frac{\mathrm{d}M_7}{\mathrm{d}\xi},\\ &\Upsilon = M_8,\ \Upsilon' = M_9,\ \Upsilon'' = \frac{\mathrm{d}M_9}{\mathrm{d}\xi}, \end{aligned}\right\} \tag{22}$$

$$\frac{\mathrm{d}M_3}{\mathrm{d}\xi} = \frac{-\left[M_1M_3 - (M_2)^2\right]\{1 + (\mathrm{We}\ M_3)^n\}^2 - \cos\omega\lambda(M_4 - \gamma_c M_6 - \gamma_m M_8)\{1 + (\mathrm{We}\ M_3)^n\}^2}{(1 + (1-n)(\mathrm{We}\ M_3)^n)}, \tag{23}$$

$$\frac{\mathrm{d}M_5}{\mathrm{d}\xi} = \frac{-\mathrm{Pr}\ M_1M_5 - \mathrm{Pr}\ \mathrm{Nb}\ M_5M_7 - \mathrm{Pr}\ \mathrm{Nt}\ M_5^2}{\left(1 + \frac{4}{3}\mathrm{Rd}\right)}, \tag{24}$$

$$\frac{\mathrm{d}M_7}{\mathrm{d}\xi} = -\mathrm{Sc}\ M_1M_7 - \frac{\mathrm{Nt}}{\mathrm{Nb}}\left[\frac{\mathrm{d}M_5}{\mathrm{d}\xi}\right] + \mathrm{Sc}\ \mathrm{Kr}\ M_6, \tag{25}$$

$$\frac{\mathrm{d}M_9}{\mathrm{d}\xi} = -\mathrm{Lb}\ M_1M_9 + \mathrm{Pe}\left[M_9M_7 + \frac{\mathrm{d}M_7}{\mathrm{d}\xi}(M_8 + \Omega)\right]. \tag{26}$$

Subject to the BC's

$$\left.\begin{aligned} &M_1 = 0,\ M_2 = 1,\ M_5 = -\mathrm{Bi}(1 - M_4),\ M_6 = 1,\\ &M_8 = 1\ \text{as}\ \xi = 0\\ &M_2 \to 0,\ M_4 \to 0,\ M_6 \to 0,\ M_8 \to 0\ \text{as}\ \xi \to \infty. \end{aligned}\right\} \tag{27}$$

To numerically solve these equations, seven initial conditions are required. The function F is given two initial conditions, while ϑ, Φ, and Υ each have one initial condition. The shooting technique is active to calculate the three remaining initial conditions, which are dependent on the three end conditions. An essential element of the shooting approach involves choosing a sensible approximation for ξ_∞. Commence the process of determining the ξ_∞ value for the BVP by generating initial approximations for specific physical parameter configurations in order to obtain $F''(0)$, $\vartheta'(0)$, $\Phi'(0)$, and $\Upsilon'(0)$. Utilizing the Bvp4c method to solve the system of seven simultaneous equations to conveniently obtain the $F''(0)$, $\vartheta'(0)$, $\Phi'(0)$, and $\Upsilon'(0)$ fields corresponding to a specific set of physical parameters. The variable step size $\xi_\infty = 0.001$ is employed in this process, which was iterated until the result approached the tolerance level of 10^{-6} asymptotically.

5 ANN model

An ANN utilizes a complex network of artificial neurons to link input and output variables, resulting in impressive results in evaluation methods. ANNs surpass conventional tools in terms of their exceptional speed, extensive capacity, and user-friendly characteristics, resulting in their extensive integration across various technological areas. These models offer pragmatic and cost-effective approaches for simulating intricate problems.

ANNs possess the capability to acquire knowledge from previous encounters and effectively tackle complex problems that involve nonlinear relationships, hence enabling the creation of various system architectures. This versatility has been employed in several industries including banking, healthcare, and engineering. Within an ANN, a neuron compute unit can represent items such as attributes, characters, concepts, or generalizations. The network is composed of three distinct types of computing units: input, output, and hidden components.

In addition, the multi-layer perceptron (MLP) is a widely used ANN model that employs a feed-forward back-propagation framework. A MLP network consists of an input layer with defined input parameters, an output layer that generates predicted values, and at least one hidden layer. The connectivity between each layer is achieved through the utilization of a transfer function, whereas the hidden layer consists of neurons, which are also referred to as processing cells. Each succeeding layer consists of a set quantity of neurons.

Scientists are becoming more interested in the prediction capacities of artificial intelligence, especially in the field of fluid science. Within this context, the examination focuses on 10 neurons located in the hidden layer. This is illustrated in Figure 2, which depicts the ANN model. The utilization of ANNs for addressing the current challenge will be examined in the subsequent section.

Metrics like mean square error (MSE) and the coefficient of determination (R) are used to assess the predictive performance of MLP models. The equations employed to compute MSE and R principles are essential for evaluating the effectiveness of the ANN model. MSE and regression analysis are essential for evaluating the efficacy of the ANN model, as described by the subsequent relationships:

$$\text{Mean Sq error (MSE)} = \frac{1}{M}\sum_{i=1}^{N}(X_{\text{num}(i)} - X_{\text{ANN}(i)})^2, \quad (28)$$

$$R = \sqrt{1 - \frac{\sum_{i=1}^{N}(X_{\text{num}(i)} - X_{\text{ANN}(i)})^2}{\sum_{i=1}^{1}(X_{\text{num}(i)})^2}}. \quad (29)$$

6 Graph and discussion

This section explores the significance of key characteristics in various profiles, including velocity, temperature, concentration, motile density, entropy generation, and the Bejan number. Figures and tables are used to investigate the characteristics of these metrics. We have utilized both the bvp4c method and the ANN based on the Levenberg–Marquardt algorithm model for this research problem. The output of the artificial intelligence neural network (AINN) model is compared to the target values and analyzed. The findings of our study demonstrate that the ANN model is accomplished of precisely forecasting the output values.

6.1 Velocity field

Figure 3(a)–(e) show the training outcomes of the ANN for the velocity profile by utilizing the Levenberg–Marquardt algorithm. Figure 3(a) illustrates the progression of training, validation, and testing data over the epochs. The graph shows that the training data performs exceptionally well during the 517th epoch, with an MSE of 3.464×10^{-9}. Figure 3(b) depicts the error distribution computed from the zero axis, elucidating the disparities between the anticipated and desired values. The analysis reveals that the zero error is measured at -4.3×10^{-6}. Figure 3(c) illustrates the gradient (9.9815×10^{-8}), Mu (1×10^{-8}), and the observation that validation checks reach zero after 517 epochs. Figure 3(d) shows a comparison between the data acquired via the bvp4c method and the data anticipated by the AINN. The comparison reveals that the predictions made by the AINN closely align with the findings received from the bvp4c approach. Figure 3(e) displays the regression plot of the developed AINN model. The regression values for the training, validation, and test phases are all equal to 1, indicating a flawless linear correlation between the input and output. These statistics collectively confirm the effectiveness of the specified ANN model. The computations are conducted using the specified parameters. The values of the variables are as follows: We = 0.1, n = 0.8, λ = 0.1, $\omega = \frac{\pi}{6}$, γ_c = 0.5, γ_m = 0.3, Rd = 0.1, Pr = 1.3, δ = 0.01, Nb = 0.1, Nt = 0.1, Sc = 0.7, Kr = 0.1, Lb = 0.9, Pe = 0.5, Ω = 0.2. and Bi = 0.5. The range of variables are $1.0 \le \text{We} \le 2.3$, $0.1 \le \lambda \le 1.1$, $0.3 \le \gamma_m \le 1.2$, $\frac{\pi}{2} \le \omega \le \frac{\pi}{6}$, $1.1 \le \text{Nt} \le 2.0$, $0.1 \le \text{Nb} \le 0.4$, $0.1 \le \text{Rd} \le 0.9$, $0.1 \le \text{Bi} \le 0.4$, $0.1 \le \text{Bi} \le 0.4$, $1.1 \le \text{Pr} \le 1.9$, $1.1 \le \text{Sc} \le 2.4$, $1.0 \le \text{Kr} \le 2.4$, $1.0 \le \text{Pe} \le 2.4$, $1.0 \le \text{Lb} \le 2.4$, $0.1 \le \text{Br} \le 1.6$, $0.1 \le \beta_1 \le 0.4$, $0.11 \le \beta_2 \le 0.14$, $0.1 \le L \le 0.4$.

Figure 4(a) shows the influence of the Weissenberg number (We) on the velocity profile $F'(\xi)$. An augmentation in We results in an upward displacement of the velocity profile. The reason for this is that an expansion in the Weissenberg number enhances the fluid velocity of particles. In this situation, a longer material relaxation period decreases the resistance of the fluid stream, hence increasing the velocity gradient. Figure 4(b) investigates the characteristics of the mixed convective variable (λ) through the velocity field $F'(\xi)$. Augmenting the values of λ intensifies the velocity gradient $F'(\xi)$. As the values of the mixed convection magnitude (λ) grow, the inertial force is counteracted by the buoyancy force, increasing the velocity profile $F'(\xi)$. Figure 4(c) illustrates the impact of the bioconvection constant (γ_m) on the velocity field $F'(\xi)$. The velocity field $F'(\xi)$ exhibits greater acceleration

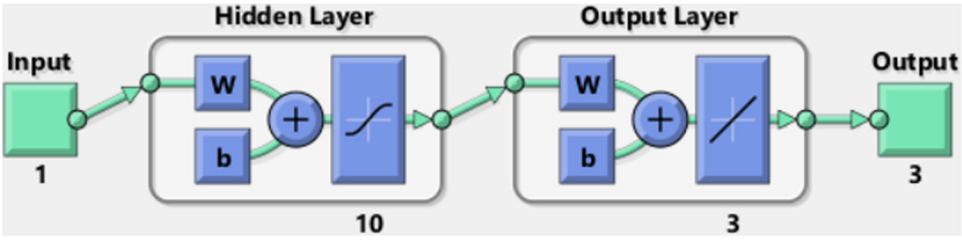

Figure 2: ANN model with input and output.

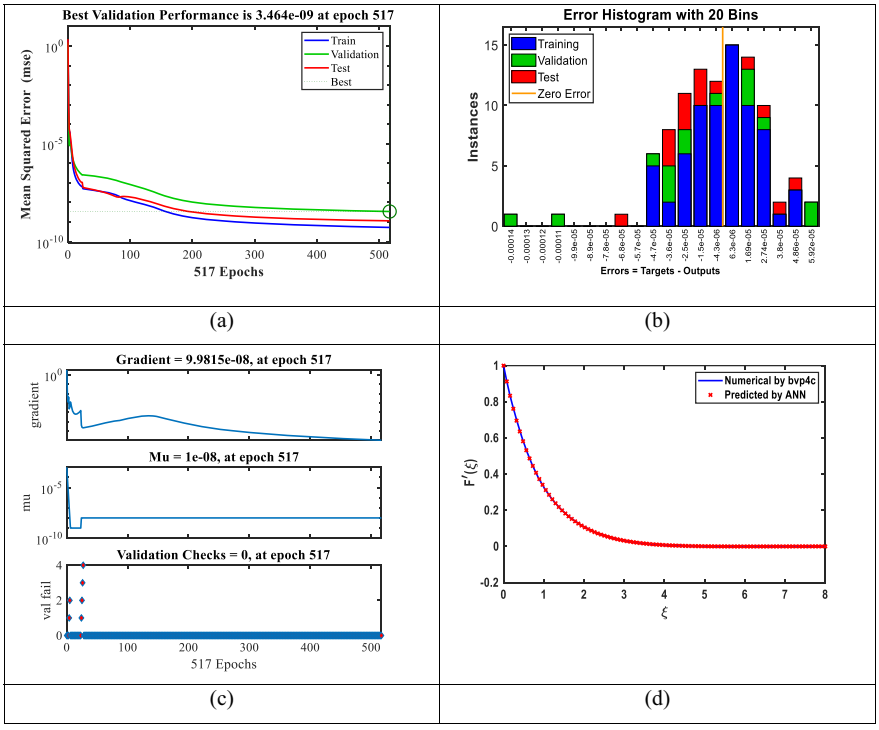

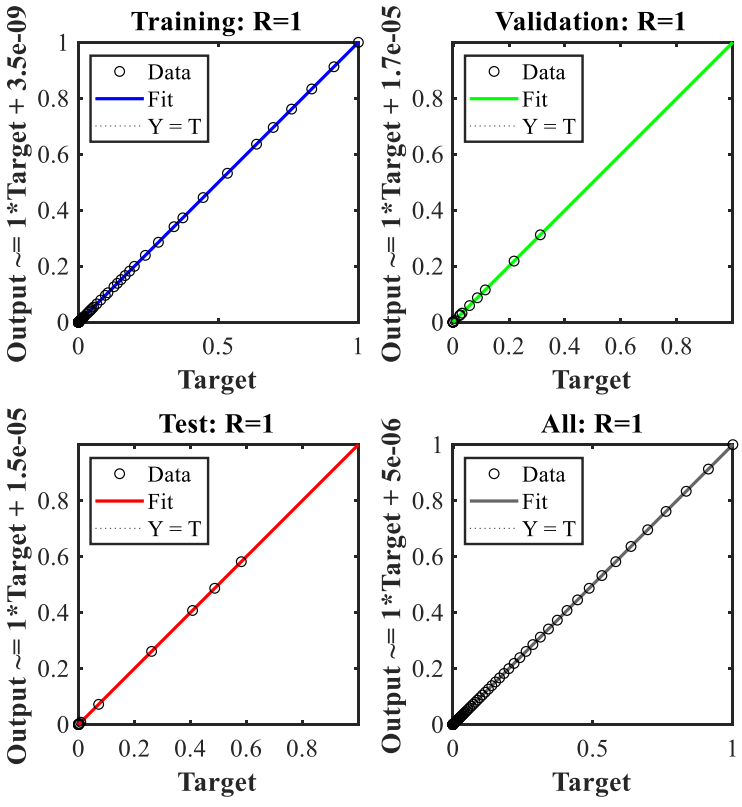

(e)

Figure 3: Graphical representation of ANN training for velocity profile: (a) performance plot, (b) error histogram, (c) transition state analysis, (d) comparison of bvp4c and ANN, and (e) regression plot.

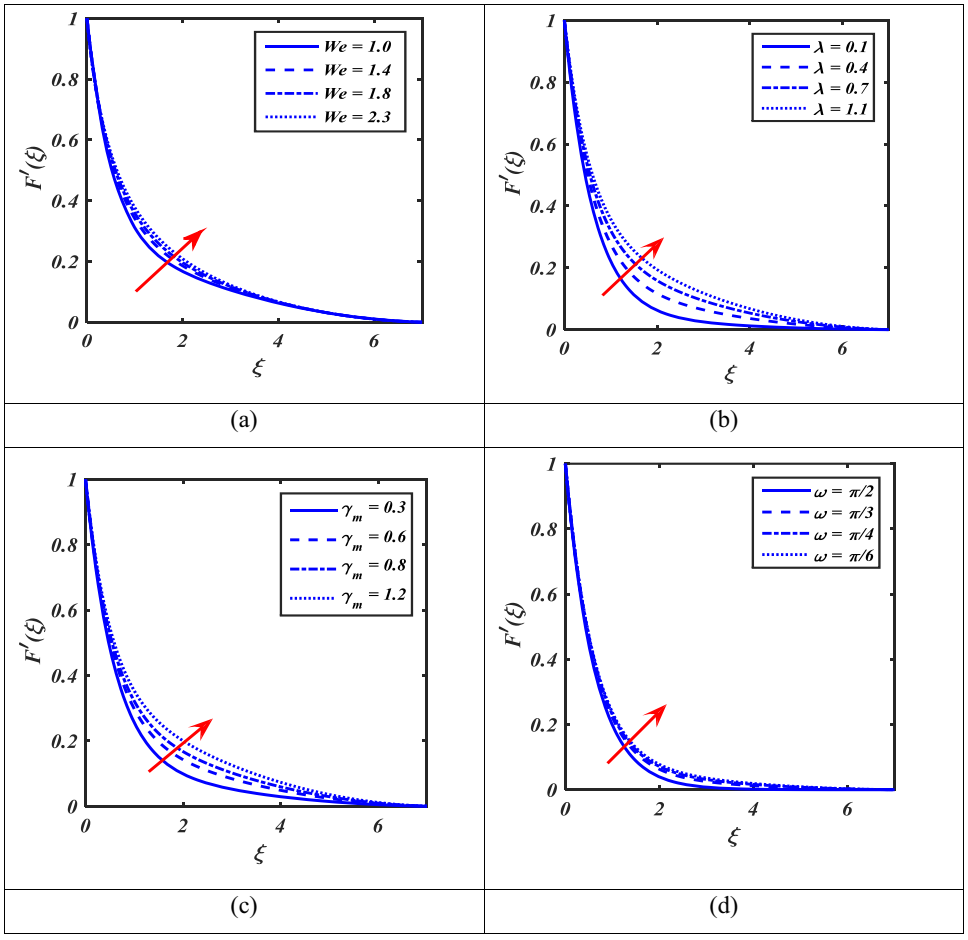

Figure 4: (a)–(d) Significant of $F'(\xi)$ versus We, λ, γ_m, and ω.

as the values of γ_m increase. The rise is attributed to the relationship between γ_m and the buoyancy force associated with bioconvection, which leads to an augmentation in the momentum field. Figure 4(d) illustrates the influence of the angle of inclination (ω) on the velocity field $F'(\xi)$. The results indicate that an augmentation in the angle of inclination (ω) boosts the velocity of the fluid motion.

6.2 Thermal characteristics

Figure 5(a)–(e) demonstrate the performance and precision of the trained ANN for the temperature profile by utilizing the Levenberg–Marquardt method. These graphs jointly illustrate the strength and efficiency of the selected ANN model. Figure 5(a) illustrates the evolution of MSE for the training, validation, and testing datasets throughout various epochs. The MSE is a crucial metric that quantifies the level of agreement between the model's predictions and the observed data. During the 505th epoch, the training data attain an extraordinarily low MSE of 2.2293×10^{-9}. This little mistake indicates that the model has successfully acquired the fundamental patterns in the training data with great proficiency, resulting in a high level of accuracy. Figure 5(b) displays the error distribution calculated from the zero axis, emphasizing the disparities between the expected and actual values. The negligible zero error, assessed at -4.32×10^{-6}, signifies that the model's predictions closely align with the actual results. A tight error distribution centered around zero indicates that the model regularly produces precise predictions across various data, highlighting its dependability. Figure 5(c) depicts the gradient value (9.9049×10^{-8}), the Mu parameter (1×10^{-9}), and the number of validation tests during the epochs. The gradient value quantifies the inclination of the error surface and signifies the speed at which the MSE is changing. A subtle gradient indicates that the model has either attained or is in close proximity to achieving a minimum level of inaccuracy. The Mu parameter, which is associated with the algorithm's adjustment step size, has a low value that indicates precise adjustment toward the ideal solution. The

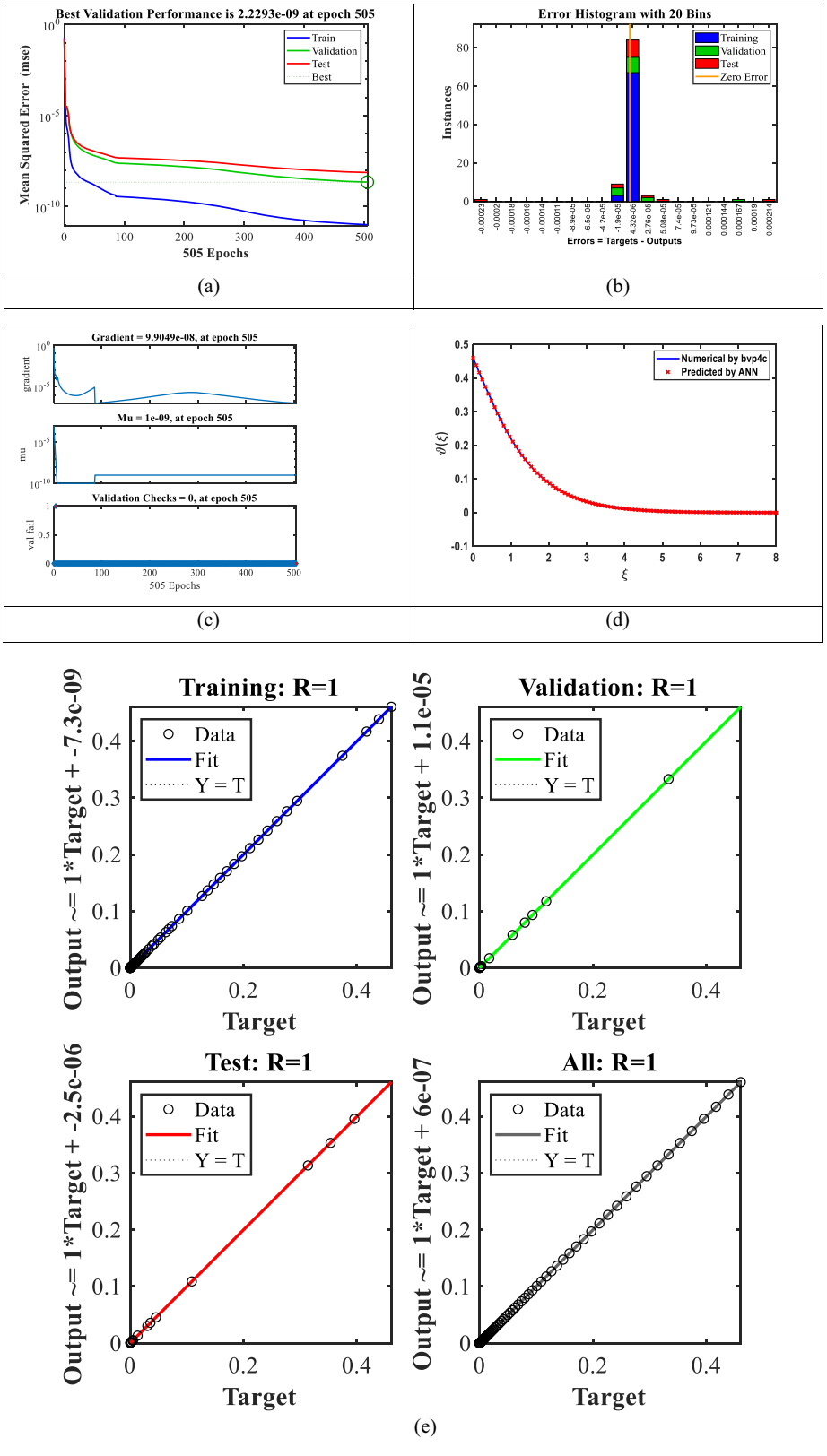

Figure 5: Graphical representation of ANN training for temperature profile: (a) performance plot, (b) error histogram, (c) transition state analysis, (d) comparison of bvp4c and ANN, and (e) regression plot.

validation checks reaching zero after 505 epochs indicates that there is no further enhancement in the validation error. This confirms that the model has converged and is not suffering from overfitting. Figure 5(d) presents a comparison between the temperature profile data produced using the bvp4c approach and the predictions made by the ANN. The strong correlation between the two datasets suggests that the ANN's forecasts are extremely precise. This agreement confirms the ANN's capacity to accurately simulate the temperature profile, showcasing its dependability in reproducing intricate physical phenomena. Figure 5(e) displays a regression figure that demonstrates the correlation between the network outputs and the relevant targets for the training, validation, and test datasets. All the regression values (R-values) for these phases are identical, suggesting a flawless linear correlation between the inputs and outcomes. The high R-values indicate that the ANN has successfully learned the mapping function and can make precise predictions for the outputs. The graphical studies provide strong evidence for the reliability and efficacy of the selected ANN model. The computations were performed using the following parameters: We = 0.1, n = 0.8, λ = 0.1, $\omega = \frac{\pi}{6}$, γ_c = 0.5, γ_m = 0.3, Rd = 0.1, Pr = 1.3, δ = 0.01, Nb = 0.1, Nt = 0.1, Sc = 0.7, Kr = 0.1, Lb = 0.9, Pe = 0.5, Ω = 0.2 and Bi = 0.5. The parameters establish the model's criteria and limitations, guaranteeing that the ANN's forecasts are pertinent and suitable for the specific physical situation.

Figure 6(a) and (b) illustrate the role of the thermophoretic variable (Nt) and the Brownian movement (Nb) on the thermal behavior $\vartheta(\xi)$. The objective of Figure 6(a) is to explore the role of the thermophoretic variable (Nt) on $\vartheta(\xi)$. An increase in thermal intensity $\vartheta(\xi)$ has been seen, functioning to the thermal curve. This is due to the intensified thermophoretic action, causing the nanoparticles to move from the hot fluid to the cooler surrounding fluid. Figure 6(b) demonstrates that the function $\vartheta(\xi)$ for (Nb) has a comparable pattern. The role of the radiative variable (Rd) across the thermal layer $\vartheta(\xi)$ may be seen in Figure 6(c). It is observed that higher values of (Rd) lead to an increase in $\vartheta(\xi)$. From a physical standpoint, an increase in (Rd) results in a greater transmission of heat energy in the flow. Consequently, the structure undergoes cooling, allowing the fluid to extract thermal energy from the flow zone. This is consistent with the general pattern of the thermal radiation parameter. Figure 6(d) illustrates the distinct impact of the Biot number on a thermal gradient. In this scenario, the heat transfer is enhanced by higher Bi values, elucidating the physical mechanism by which greater rate of heat travels to the nanoparticles from the surface, resulting in an increased temperature gradient. Figure 6(e) depicts the role of the Prandtl number (Pr) on the thermal field. The thermal gradient diminishes as the Prandtl number (Pr) increases. Greater (Pr) values result in reduced thermal diffusivity, whereas lower values are linked to increased thermal diffusivity. This means to a lessening in thermal curve. The progressive reduction in the thickness of the border layer is a defining feature of shear thickening behavior. Furthermore, the thermal profile diminishes due to the inverse correlation between (Pr) and thermal diffusivity, as defined.

6.3 Concentration characteristics

Figure 7(a)–(e) demonstrate the performance and accuracy of the trained AINN for the concentration profile. The Levenberg–Marquardt approach is used to achieve this, highlighting the model's robustness and effectiveness. Figure 7(a) displays the MSE for the training, validation, and testing datasets at different epochs. The training data achieve an exceptionally low MSE of (4.5321×10^{-9}) at the 808th epoch. This demonstrates the model's exceptional precision in acquiring knowledge of the data patterns. Figure 7(b) displays the error distribution starting from the zero axis, showing a minimal zero error of (4.35×10^{6}), which suggests accurate predictions. Figure 7(c) displays the gradient value (9.9323×10^{-8}), the Mu parameter (1×10^{-9}), and the validation checks, indicating that the model has successfully converged without overfitting. Figure 7(d) presents a comparison between the concentration profile data obtained via the bvp4c approach and the predictions made by the ANN. This comparison shows a significant correlation, which confirms the correctness of the ANN. Figure 7(e) displays a regression plot indicating R-values of 1 for the training, validation, and test datasets, which confirms a flawless linear relationship and accurate predictions. The graphical analyses confirm the reliability and effectiveness of the ANN model, which was computed using specific parameters. These parameters include We = 0.1, n = 0.8, λ = 0.1, $\omega = \frac{\pi}{6}$, γ_c = 0.5, γ_m = 0.3, Rd = 0.1, Nb = 0.1, Pr = 1.3, δ = 0.01, Sc = 1.2, Nt = 0.1, Kr = 0.1, Lb = 0.9, Pe = 0.5, Ω = 0.2 and Bi = 0.5. These parameters ensure that the predictions made by the model are relevant and applicable. Figure 8(a) demonstrates the role of the thermophoretic variable (Nt) across the mass gradient $\Phi(\xi)$. As the thermophoretic parameter grows, the concentration gradient increases. A growth in (Nt) consequences in a higher amount of thermophoretic energy, leading to the movement of nanoparticles from hotter to cooler places. This movement generates an increase in particle concentration in the cooler

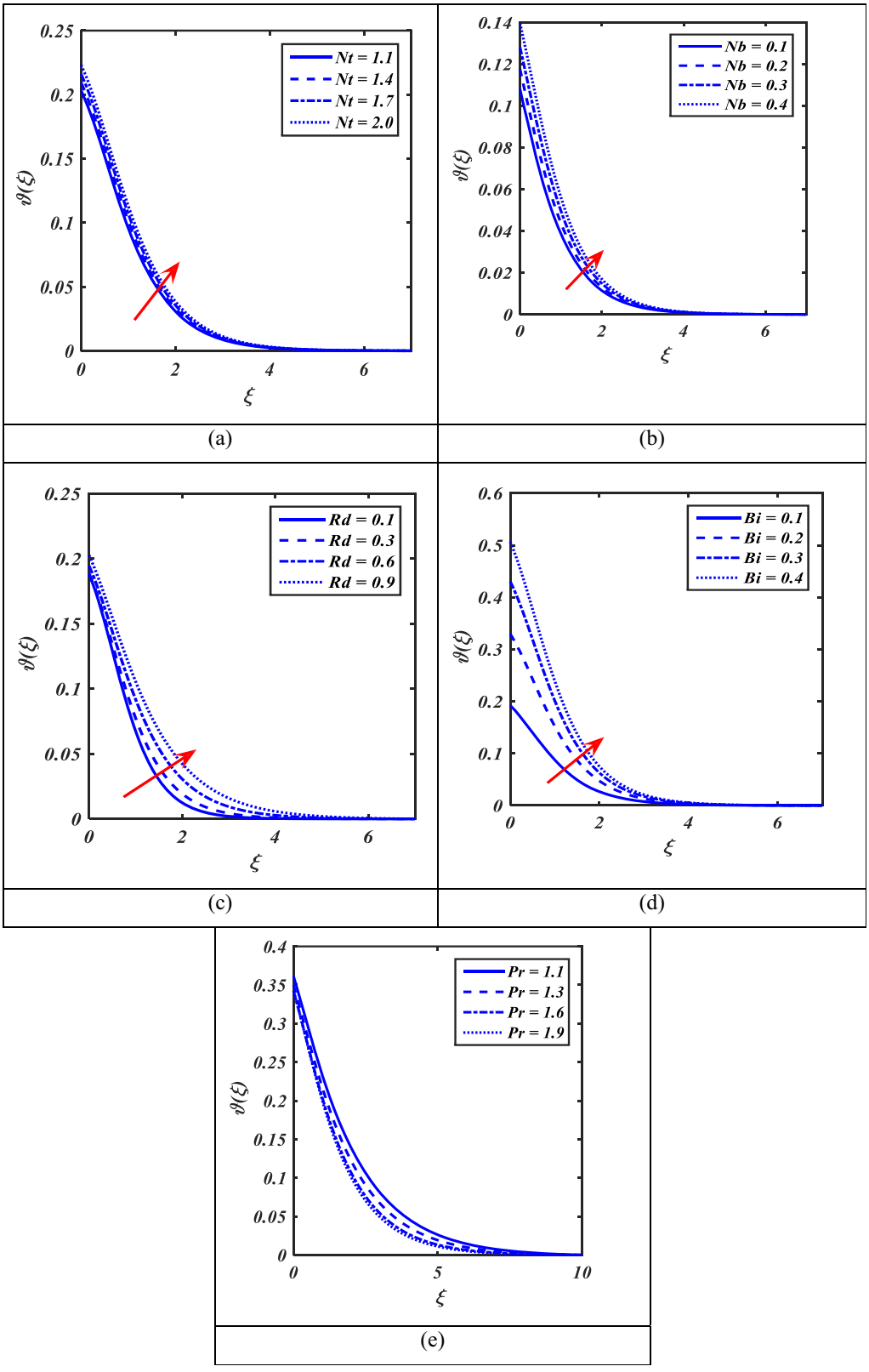

Figure 6: (a)–(e) Significant of $\vartheta(\xi)$ versus Nt, Nb, Rd, Bi, and Pr.

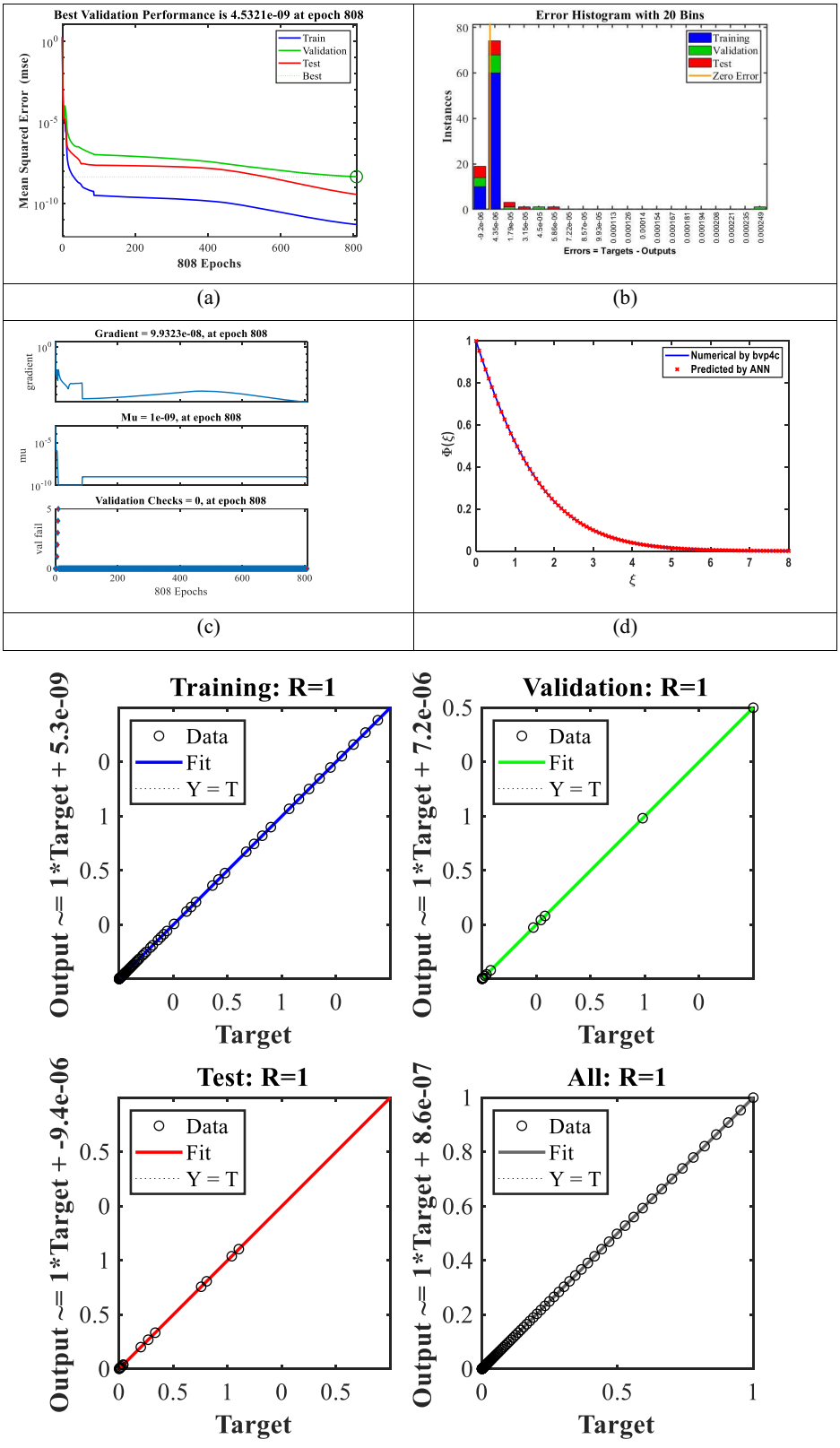

Figure 7: Graphical representation of ANN training for concentration profile: (a) performance plot, (b) error histogram, (c) transition state analysis, (d) comparison of bvp4c and ANN, and (e) regression plot.

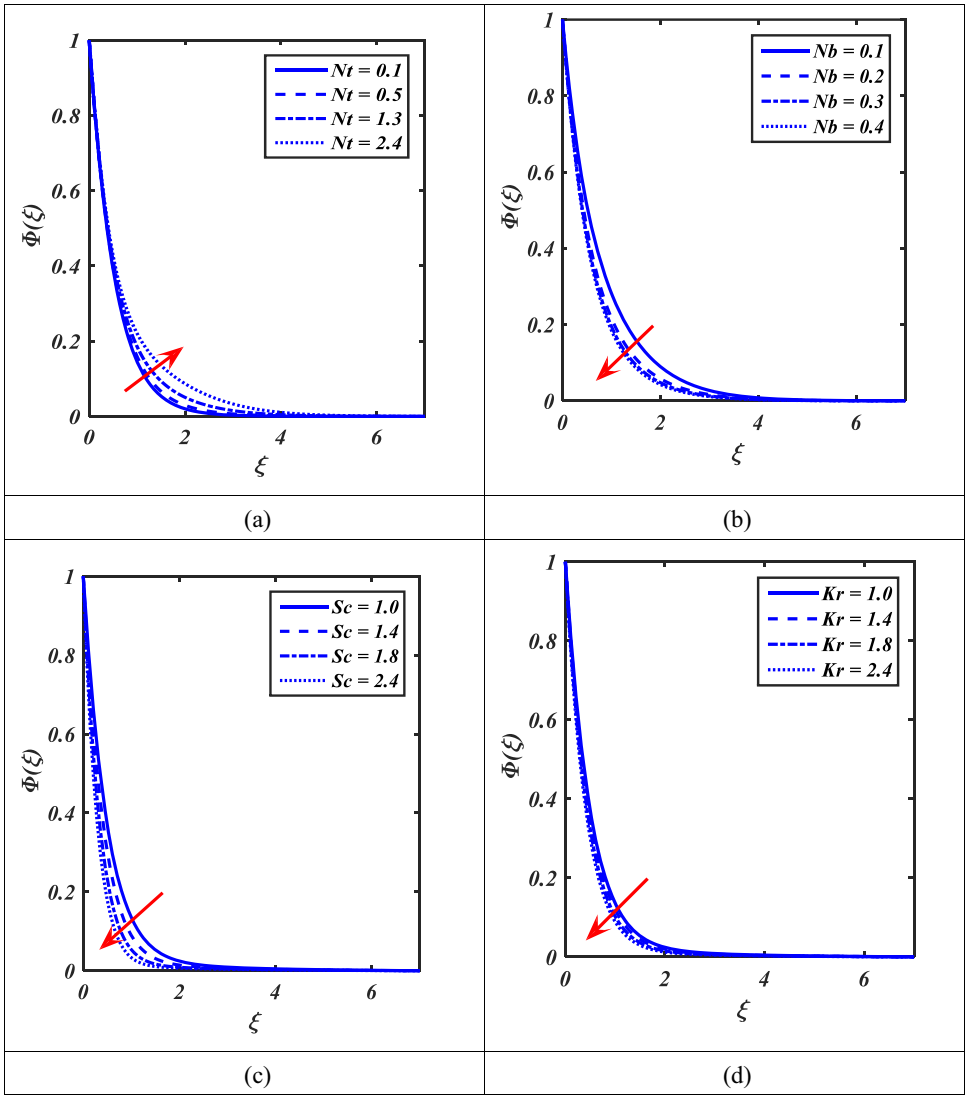

Figure 8: (a)–(d) Significance of $\Phi(\xi)$ versus Nt, Nb, Sc, and Kr.

parts. Figure 8(b) illustrates the variation in the concentration gradient $\Phi(\xi)$ in relation to the Brownian motion parameter (Nb). A growth in the quantity of Nb reduces the magnitude of the concentration gradient $\Phi(\xi)$. A growth in Nb functioning to more particle diffusion and increased collision frequency, resulting in a reduction in the rate of mass of the fluid. Figure 8(c) illustrates the decreasing relationship between the Schmidt number (Sc) and mass transfer rate $\Phi(\xi)$. The Schmidt number (Sc) is a nondimensional parameter that quantifies the ratio of mass diffusion to momentum diffusion in fluid flow. A lower *Sc* value indicates a greater abundance of nanoparticles. Figure 8(d) demonstrates the changes in the rate of mass as the chemical reaction variable (Kr) varies. As the Kr value increases, the mass of gradient in the boundary layer drops. This phenomenon arises due to an elevated Kr value, which signifies an increased number of chemical processes that consume the species. So, lessening in the concentration gradient $\Phi(\xi)$.

6.4 Microorganism characteristics

Figure 9(a)–(e) provide a complete demonstration of the performance and accuracy of the trained AINN in predicting the microorganism profile. The Levenberg–Marquardt approach is used to highlight the model's robustness. The MSE decreases significantly throughout several epochs, as shown in Figure 9(a). At the 570th epoch, the MSE reaches an impressively low value of 9.5694×10^{-10}, indicating the outstanding precision of the ANN in learning data patterns. In addition, Figure 9(b) illustrates the

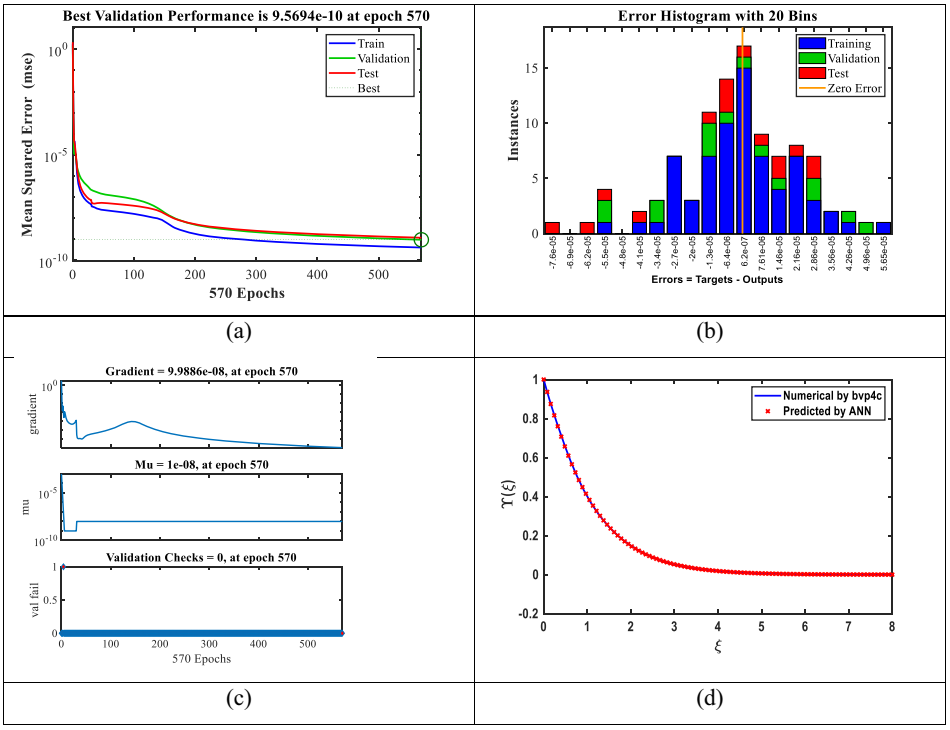

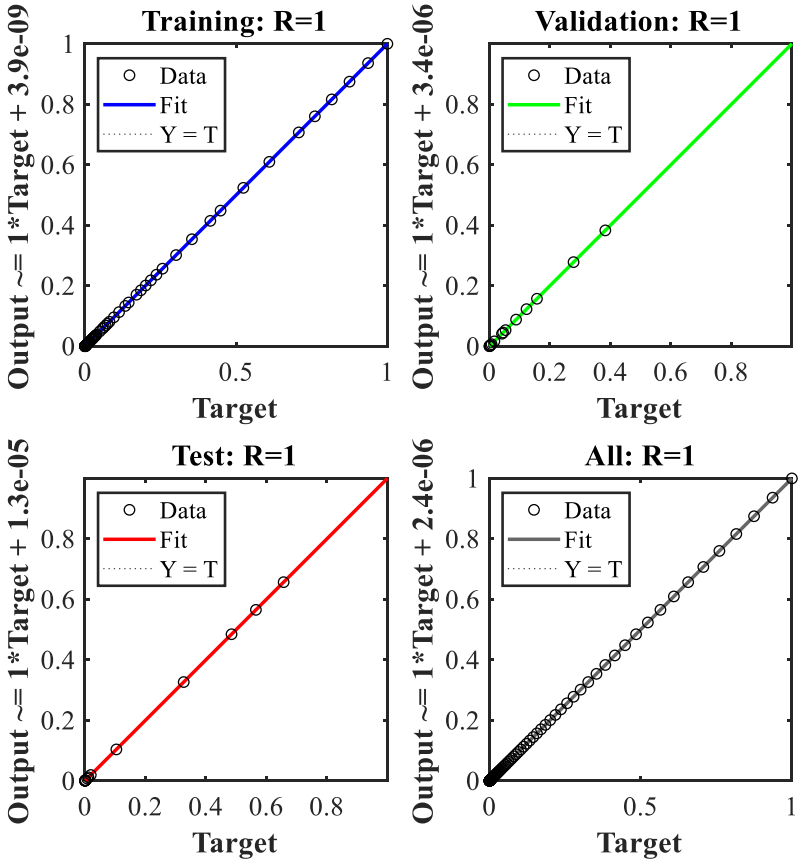

Figure 9: Graphical representation of ANN training for concentration profile: (a) performance plot, (b) error histogram, (c) transition state analysis, (d) comparison of bvp4c and ANN, and (e) regression plot.

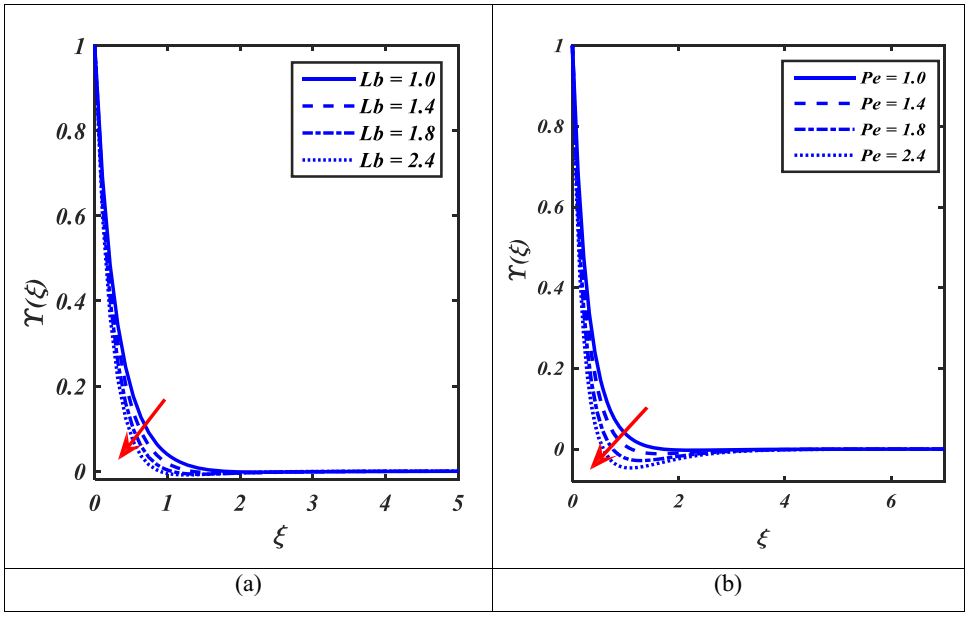

Figure 10: (a) and (b): Significant of $\Upsilon(\xi)$ versus Lb and Pe.

distribution of errors, which are centered around zero. The minimum error, which is close to zero, is 6.2×10^{-7}, illustrating the model's exceptional precision in making predictions. In addition, Figure 9(c) provides specific information about the gradient value (9.9886×10^{-8}), the Mu parameter (1×10^{-8}), and the validation checks. These features combined indicate that the model has successfully converged and has avoided overfitting. The strong agreement between the microorganism profile data predicted by the ANN and the data collected using the bvp4c approach, as shown in Figure 9(d), confirms the dependability and accuracy of the ANN. The regression diagram in Figure 9(e) demonstrates a perfect linear relationship between the inputs and outputs of the model, as indicated by *R*-values of 1 for the training, validation, and test datasets. This supports the model's exact prediction capabilities. The parameters utilized for these computations are as follows: We = 0.1, n = 0.8, λ = 0.1, $\omega = \frac{\pi}{6}$, γ_c = 0.5, γ_m = 0.3, Nb = 0.1, Rd = 0.1, Pr = 1.3, δ = 0.01, Nt = 0.1, Kr = 0.1, Sc = 1.2, Lb = 0.9, Pe = 0.5, Ω = 0.2 and Bi = 0.5 verify that the model's predictions are pertinent and suitable for the specific physical situation, hence reinforcing the usefulness and dependability of the ANN.

Figure 10(a) illustrates the changes in the motile microbe profile $\Upsilon(\xi)$ due to the magnitude of bioconvection Lewis number (Lb). A higher bioconvection Lewis number (Lb) leads to an upsurge in the profile of motile microbes $\Upsilon(\xi)$. The Peclet number (Pe) and the microorganism field $\Upsilon(\xi)$ are exemplified in Figure 10(b). A higher Peclet number (Pe) results in a decreased motile microbe profile $\Upsilon(\xi)$. This phenomenon arises due to a larger Peclet number (Pe), which leads to a reduce in the motile density $\Upsilon(\xi)$ of the fluid by reducing the diffusivity of the microorganisms.

6.5 Entropy generation and Bejan number characteristics

Figure 11(a) illustrates the relationship between the Weissenberg parameter (We) and entropy generation $\mathrm{Ns}(\xi)$. The production of entropy reduces as the Weissenberg parameter (We) values grow. Figure 11(b) illustrates that the rising values of the Brinkman number (Br) increases the entropy generation $\mathrm{Ns}(\xi)$. The Brinkman number (Br) quantifies the transfer of heat through the combination of viscous flow and molecular conduction in processes such as polymer production. Molecular conduction is significantly more efficient in transporting heat compared to heat propagation through viscous effects. Figure 11(c) illustrates the impact of β_1 on $\mathrm{Ns}(\xi)$. The function $\mathrm{Ns}(\xi)$ demonstrates a positive correlation with β_1. Figure 11(d) depicts the characteristics of β_2 on $\mathrm{Ns}(\xi)$. Here, a higher value of β_2 causes a decrease in the influence of $\mathrm{Ns}(\xi)$. As β_2 (temperature ratio parameter) grows, the temperature differential within the system also increases, resulting in a bigger temperature gradient. The elevated temperature difference leads to an increased rate of entropy production as a result of the heightened level of irreversibility in the heat transfer phenomenon. As the temperature ratio parameter (β_2) grows, the system's entropy generation also increases.

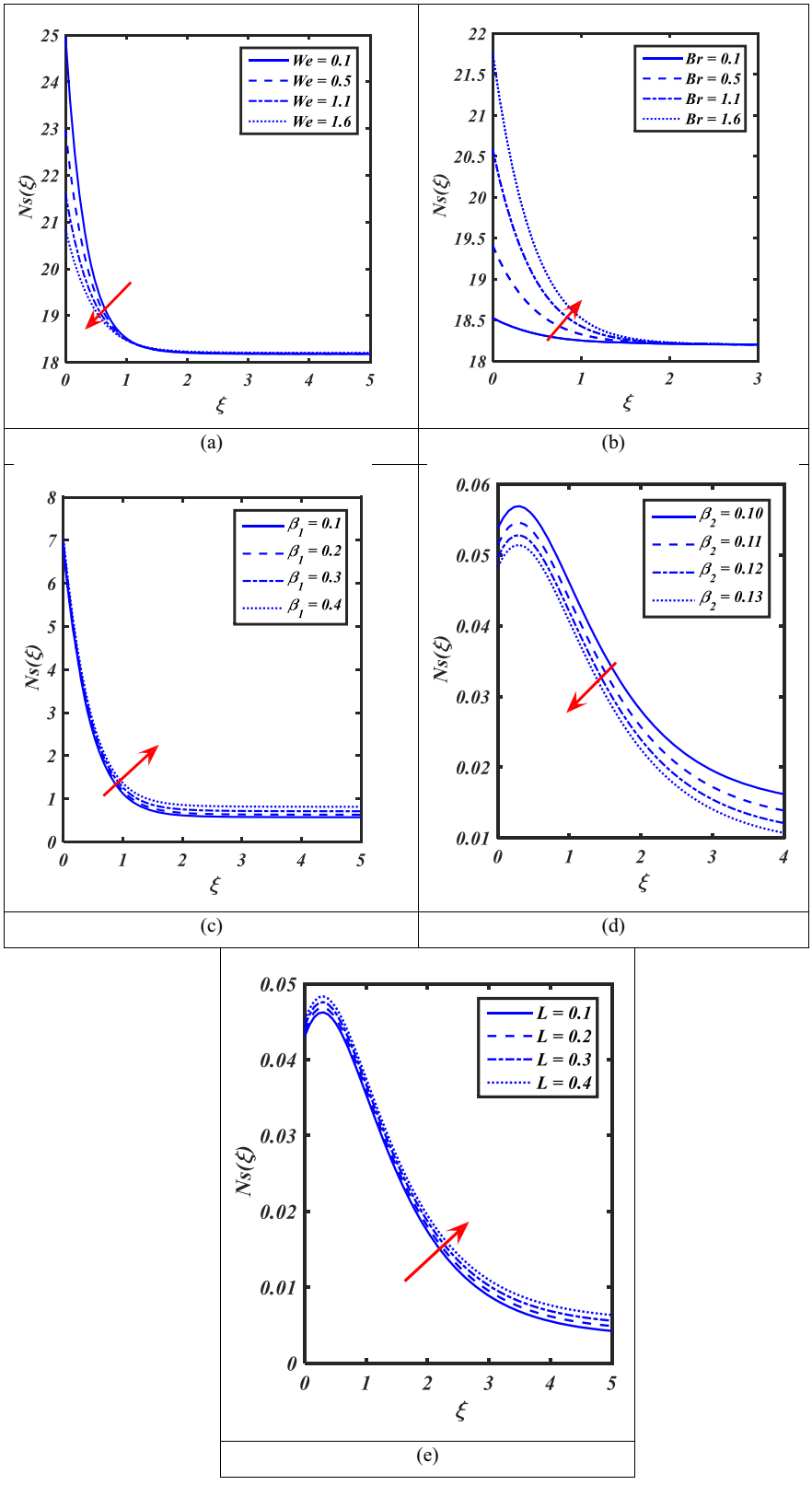

Figure 11: (a)–(e) Significant of Ns(ξ) versus We, Br, β_1, β_2, and L.

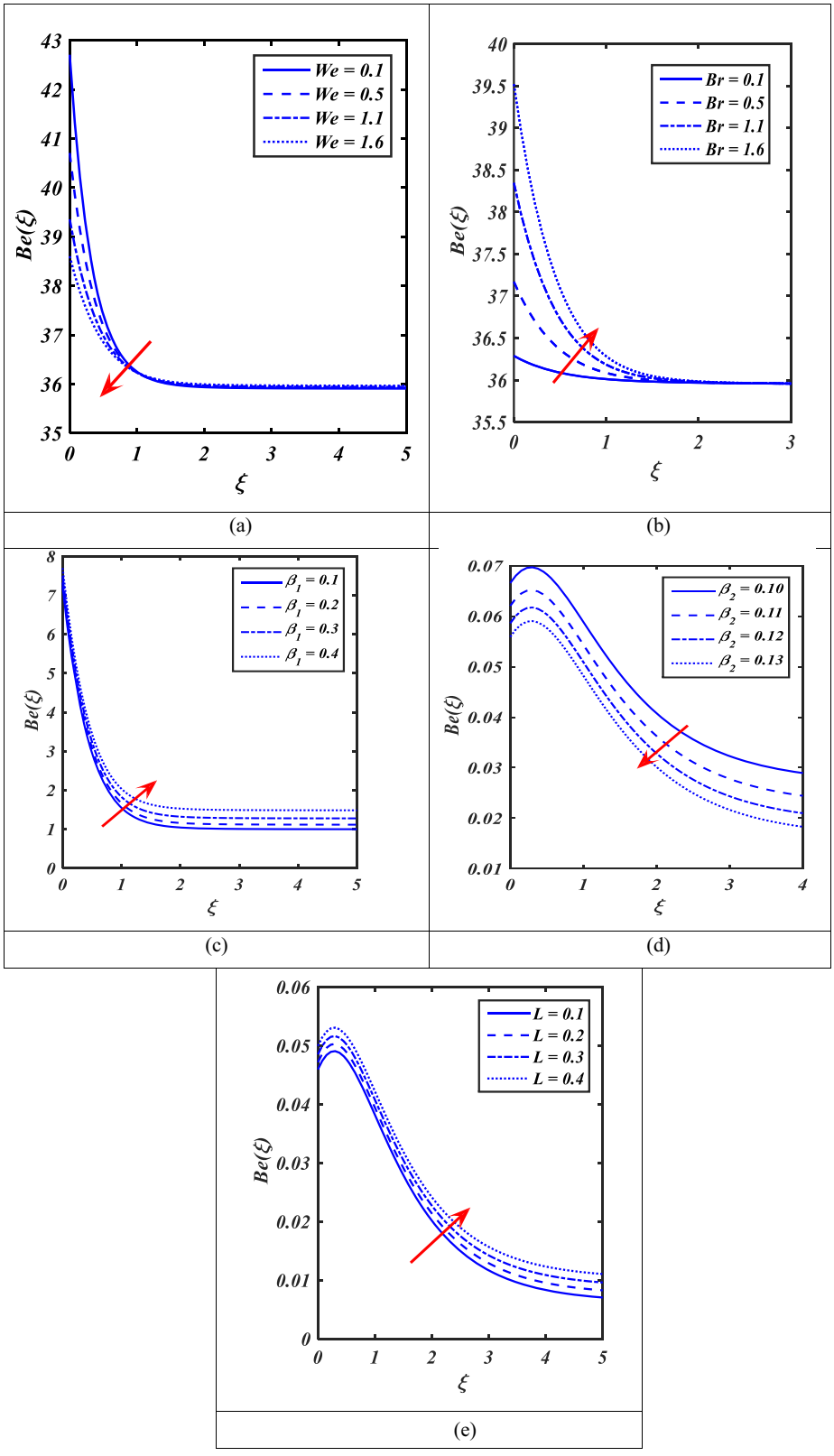

Figure 12: (a)–(e) Significant of Be(ξ) versus We, Br, β_1, β_2 and L.

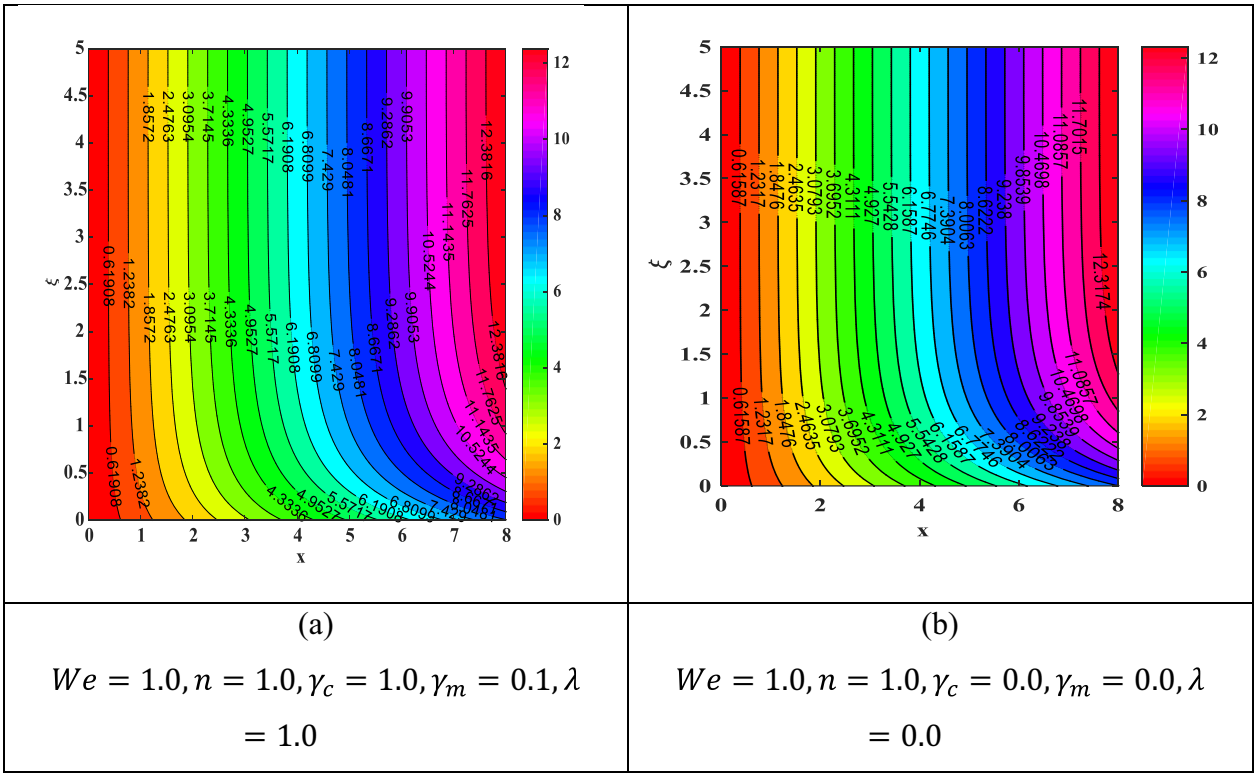

Figure 13: Streamline sketch for various values of We, λ, γ_m, γ_c, n. (a) We = 1.0, n = 1.0, γ_c = 1.0, γ_m = 0.1, λ = 1.0. (b) We = 1.0, n = 1.0, γ_c = 0.0, γ_m = 0.0, λ = 0.0.

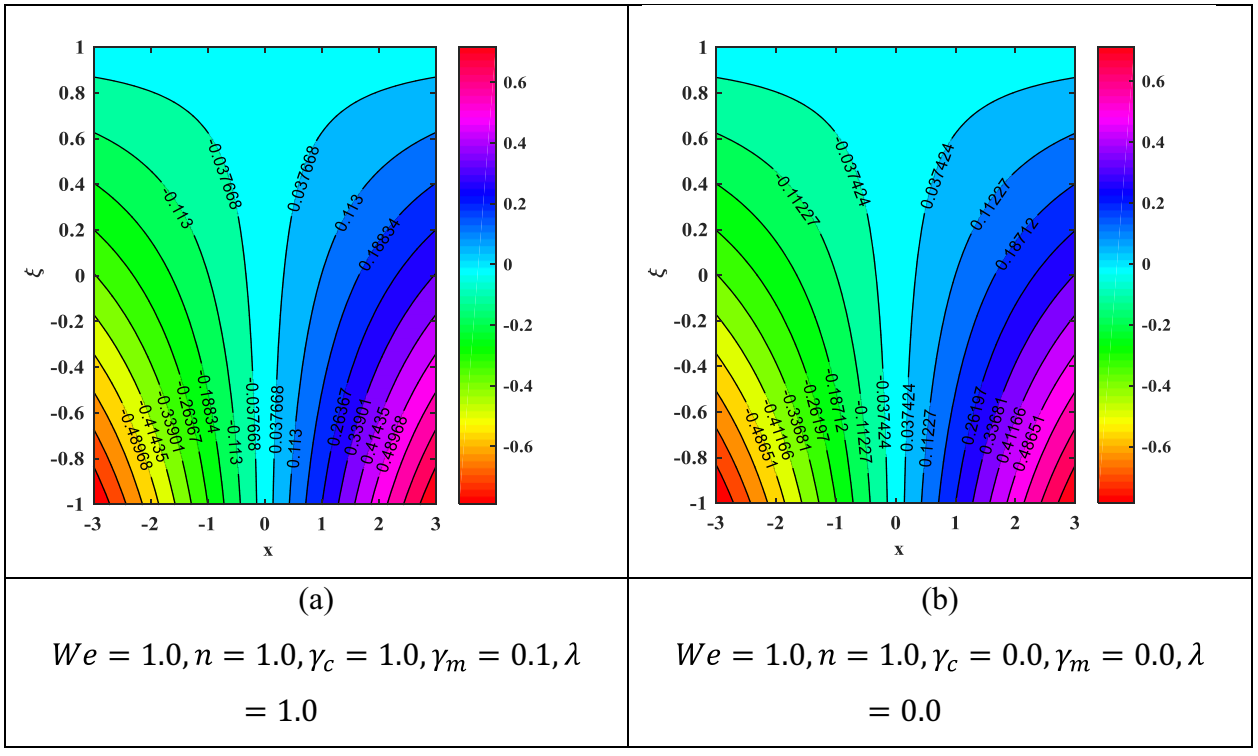

Figure 14: Isotherm line sketch for various values of We, λ, γ_m, γ_c, n. (a) We = 1.0, n = 1.0, γ_c = 1.0, γ_m = 0.1, λ = 1.0. (b) We = 1.0, n = 1.0, γ_c = 0.0, γ_m = 0.0, λ = 0.0.

Table 1: Magnitude of $\mathrm{Re}_x^{1/2}C_{fx}$ for different values of the We, n, λ, γ_m and γ_c

We	n	λ	γ_m	γ_c	ω	$\mathrm{Re}_x^{\frac{1}{2}}$ Cf(bvp4c)	$\mathrm{Re}_x^{\frac{1}{2}}$ Cf(ANN)
0.1	0.8	0.1	0.3	0.5	$\pi/6$	−1.2657	−1.2657
0.2						−1.5949	−1.5948
0.3						−2.1088	−2.0962
0.4						−3.0469	−3.0461
	0.1					−3.3819	−3.3446
	0.3					−3.3027	−3.3025
	0.5					−3.2138	−3.2134
	0.7					−3.1074	−3.1072
		0.2				−3.2744	−3.2735
		0.3				−3.4554	−3.4546
		0.4				−3.6532	−3.5800
		0.5				−3.8717	−3.8710
			0.1			−3.3054	−3.3052
			0.2			−3.5660	−3.5658
			0.3			−3.8717	−3.8711
			0.4			−4.2574	−4.2571
				0.1		−2.9521	−2.9520
				0.2		−3.1957	−3.1956
				0.3		−3.4777	−3.4770
				0.4		−3.8149	−3.8145
					π	−2.2586	−2.2583
					$\pi/2$	−2.9525	−2.9521
					$\pi/3$	−3.4093	−3.4086
					$\pi/4$	−3.6297	−3.6284

Figure 11(e) investigates the influence of the temperature ratio parameter (L) on Ns(ξ).

The impact of We on the behavior of Be(ξ) is illustrated in Figure 12(a). The graphic illustrates that an increase in We are functioning in the Bejan number. Figure 12(b) illustrates the relationship between Be(ξ) and the fluctuation of Br in terms of Bejan number. As the Brinkman number Br increases, the level of chaos in the process also increases. Figure 12(c) establishes the influence of the concentration difference parameter β_1 on the development of Be(ξ). The rise in Bejan number Be(ξ) is observed through an increase in the concentration difference parameter β_1. Figure 12(d) reveals the attributes of β_2 on Be(ξ). It is observed that the Bejan number Be(ξ) declines when the magnitude β_2 is increased. The increase in β_2 consequences in a more solid thermal layer, which leads to a reduction in resistance in liquid flow and a depreciation in Bejan number Be(ξ). Figure 12(e) depicts the attributes of L on Bejan number Be(ξ). In this case, the Bejan number Be(ξ) is enhanced with the use of a bigger L. The temperature of a liquid increases by way of the magnitude of L rises, bigger rate of Bejan number Be(ξ).

Figures 13(a), (b) and 14(a), (b) reveal that the streamlines of the liquid travel a more direct route, which frequently produces a smoother and steadier flow pattern. The existence of spaces in material with porosity results

Table 2: Magnitude of $\mathrm{Re}_x^{-1/2}\mathrm{Nu}_x$ for different values of the δ, Nt, Nb, Pr, Bi and Rd

Nb	Nt	Pr	Bi	Rd	δ	$-\mathrm{Re}_x^{-\frac{1}{2}}\mathrm{Nu}_x$(bvp4c)	$-\mathrm{Re}_x^{-\frac{1}{2}}\mathrm{Nu}_x$(ANN)
0.1	0.1	1.3	0.5	0.1	0.01	0.2898	0.2892
0.3						0.2773	0.2773
0.5						0.2609	0.2608
0.7						0.2436	0.2438
	0.2					0.2403	0.2403
	0.3					0.2369	0.2369
	0.4					0.2336	0.2335
	0.5					0.2302	0.2301
		0.5				0.1969	0.1966
		0.8				0.2149	0.2149
		1.1				0.2255	0.2255
		1.4				0.2320	0.2320
			0.1			0.0846	0.0845
			0.2			0.1436	0.1428
			0.3			0.1823	0.1823
			0.4			0.2106	0.2105
				0.2		0.2326	0.2326
				0.3		0.2541	0.2541
				0.4		0.2750	0.2751
				0.5		0.2956	0.2956
					0.02	0.2996	0.2997
					0.03	0.3035	0.3035
					0.04	0.3073	0.3074
					0.05	0.3110	0.3118

Table 3: Magnitude of $\mathrm{Re}_x^{-1/2}\mathrm{Sh}_x$ for different values of Kr, Nt, Nb and Sc Ω, Sc

Kr	Nt	Nb	Sc	$\mathrm{Re}_x^{-\frac{1}{2}}\mathrm{Sh}_x$(bvp4c)	$\mathrm{Re}_x^{-\frac{1}{2}}\mathrm{Sh}_x$(ANN)
0.1	0.1	0.1	0.7	0.3396	0.3396
0.2				0.4510	0.4518
0.3				0.5323	0.5329
0.4				0.6010	0.6010
	0.2			0.5144	0.5145
	0.3			0.4368	0.4372
	0.4			0.3722	0.3724
	0.5			0.3216	0.3227
		0.2		0.5005	0.5012
		0.3		0.5742	0.5742
		0.4		0.6128	0.6128
		0.5		0.6367	0.6366
			0.9	0.7538	0.7542
			1.1	0.8584	0.8584
			1.3	0.9536	0.9545
			1.5	1.0415	1.0415

in relations between the liquid inside and the material's solid matrix. This relationship may lead to modifications in the fluid velocity distribution, a boost in obstruction, and variations in the routes followed by the flowing fluid. It is evident from both figures that the fluid velocity decreased when porosity was added.

Tables 1–4 are recorded to examine the relationships between skin friction $\mathrm{Re}_x^{1/2}C_{fx}$, Nusselt $\mathrm{Re}_x^{-1/2}\mathrm{Nu}_x$, Sherwood $\mathrm{Re}_x^{-1/2}\mathrm{Sh}_x$, and microorganism $\mathrm{Re}_x^{-1/2}\mathrm{Nh}$ values and different parameters of interest for both outcomes bvp4c and ANN model. Table 1 presents the relationship between the $\mathrm{Re}_x^{1/2}C_{fx}$ of bvp4c and $\mathrm{Re}_x^{1/2}C_{fx}$ of ANN outcomes for the variables We, n, $\lambda, \gamma_c, \gamma_m$. Here, the decay of $\mathrm{Re}_x^{1/2}C_{fx}$ is

Table 4: Magnitude of $\mathrm{Re}_x^{-1/2}\mathrm{Nh}$ for different values of the Pe, Lb, Ω

Pe	Lb	Ω	$\mathrm{Re}_x^{-\frac{1}{2}}\mathrm{Nh}$(bvp4c)	$\mathrm{Re}_x^{-\frac{1}{2}}\mathrm{Nh}$(ANN)
0.5	0.5	0.1	0.6167	0.6168
0.7			0.7455	0.7455
0.9			0.8741	0.8775
1.1			1.0030	1.0032
	1.0		1.1855	1.1887
	1.5		1.3382	1.3382
	2.0		1.4715	1.4779
	2.5		1.5916	1.5916
		0.2	1.6374	1.6374
		0.3	1.6832	1.6833
		0.4	1.7289	1.7290
		0.5	1.7745	1.7782

Table 5: Comparison of $-\vartheta'(0)$ for the magnitude of Pr

Pr	Shankaralingappa [53]	Ali et al. [54]	Current studies
0.01	0.00993	0.00993	0.0099365
0.72	0.46318	0.46318	0.4631867
1	0.58231	0.5820	0.5820789
3	1.1652	1.1652	1.1652459

determined by increasing the values of We, n, λ, γ_c, γ_m for both $\mathrm{Re}_x^{1/2}C_{fx}$ of bvp4c and $\mathrm{Re}_x^{1/2}C_{fx}$ of ANN. Table 2 displays the relationship between the contribution of $\mathrm{Re}_x^{-1/2}\mathrm{Nu}_x$ of bvp4c and $\mathrm{Re}_x^{-1/2}\mathrm{Nu}_x$ of ANN variation of the variables Bi, Pr, Nb, Nt, Rd, δ. It is seen that the $\mathrm{Re}_x^{-1/2}\mathrm{Nu}_x$ of bvp4c and $\mathrm{Re}_x^{-1/2}\mathrm{Nu}_x$ of ANN increase with higher values of Nb and Pr. In Table 4, the $\mathrm{Re}_x^{-1/2}\mathrm{Sh}_x$ of bvp4c and $\mathrm{Re}_x^{-1/2}\mathrm{Sh}_x$ of ANN drops for Sc and increases for increasing Nt. Table 4 demonstrates a decrease in the value of $\mathrm{Re}_x^{-1/2}\mathrm{Nh}$ of bvp4c and $\mathrm{Re}_x^{-1/2}\mathrm{Nh}$ of ANN for Pe and Lb. Table 5 presents a comparison of $\vartheta'(0)$, for different values of Pr and Bi with the findings of Usman et al. [21]. In this study, we observed concurrence between the bvp4c solution reported here and the shooing solution described in Usman et al. [21] under the limiting conditions.

7 Conclusion

The current study examines the microorganism's flow of Cross nanoliquid past an inclined stretched sheet by considering the effects of convection conditions using an ANN model. The analysis emphasizes the phenomena of heat radiation and chemical reactions. The above equations represent a system of connected partial differential equations. Incorporated within the dimensionless system of nonlinear ODEs by appropriate transformations. The dimensionless system of ODEs is considered using the bvp4c solver in MATLAB, which utilizes the Lobatto-IIIa formula. The key findings of the analyzed are outlined below:

- The increase in λ and γ_m decelerate the speed and inertia of the fluid.
- The coefficient of determination for all three phases (training, validation, and testing) is $R = 1$.
- The velocity, thermal layer, concentration, and motile density are examined over the ANN model.
- The guessed values from the SFC ANN model for the Weissenberg number and the power law index match the real values.

- According to bvp4c and ANN both are the same for the large values of the radiation variable and Brownian motion.
- The gradual increase We in the movement of fluid particles is seen.
- The elevated magnitude of Bi and δ enhances the heat transfer.
- The rise in the radiation variable causes an increase in the thermal boundary, while the opposite tendency is observed for an increasing Prandtl number.
- The increase in Nt and Nb leads to a decrease in the concentration gradient.
- An increase in Pe and Lb negatively impacts the microorganism profile.

Acknowledgments: The authors extend their appreciation for the support received from Princess Nourah bint Abdulrahman University Researchers Supporting Project number (PNURSP2025R163), Princess Nourah bint Abdulrahman University, Riyadh, Saudi Arabia.

Funding information: Princess Nourah bint Abdulrahman University Researchers Supporting Project number (PNURSP2025R163), Princess Nourah bint Abdulrahman University, Riyadh, Saudi Arabia.

Author contributions: U.K.; F.A.; S.E.: conceptualization, methodology, software, formal analysis, validation; writing – original draft. S.S.Z.; M.F.A.: writing – original draft, data curation, investigation, visualization, validation. A.Z.: conceptualization, writing – original draft, writing – review & editing, supervision, resources. N.S.K.; validation; writing review & editing; software; conceptualization; and provided significant feedback and assisted in the revised version of the manuscript. Further, she has also supported the revision of the manuscript critically for important intellectual content.

Conflict of interest: The authors state no conflict of interest.

Data availability statement: The datasets used and/or analyzed during the current study are available from the corresponding author upon reasonable request.

References

[1] Cross, M. M. Rheology of non-Newtonian fluids: a new flow equation for pseudoplastic systems. *Journal of Colloid Science*, Vol. 20, No. 5, 1965, pp. 417–437.

[2] Haghighi, A. R., N. Pirhadi, and M. Shahbazi Asl. A Mathematical modeling for the study of blood flow as a Cross fluid through a tapered artery. *Journal of New Researches in Mathematics*, Vol. 5, No. 20, 2019, pp. 15–30.

[3] Nazeer, M. Numerical and perturbation solutions of Cross flow of an Eyring-Powell fluid. *SN Applied Sciences*, Vol. 3, No. 2, 2021, pp. 1–11.

[4] Sabir, Z., A. Imran, M. Umar, M. Zeb, M. Shoaib, and M. A. Z. Raja. A numerical approach for two-dimensional Sutterby fluid flow bounded at a stagnation point with an inclined magnetic field and thermal radiation impacts. *Thermal Science*, Vol. 186, 2020, id. 186.

[5] Yao, L., A. Grishaev, G. Cornilescu, and A. Bax. The impact of hydrogen bonding on amide 1H chemical shift anisotropy studied by Cross-correlated relaxation and liquid crystal NMR spectroscopy. *Journal of the American Chemical Society*, Vol. 132, No. 31, 2010, pp. 10866–10875.

[6] Khan, M. I., T. Hayat, M. I. Khan, and A. Alsaedi. Activation energy impact in nonlinear radiative stagnation point flow of Cross nanofluid. *International Communications in Heat and Mass Transfer*, Vol. 91, 2018, pp. 216–224.

[7] Shah, S. Z. H., A. Ayub, Z. Sabir, W. Adel, N. A. Shah, and S. J. Yook. Insight into the dynamics of time-dependent Cross nanofluid on a melting surface subject to cubic autocatalysis. *Case Studies in Thermal Engineering*, Vol. 27, 2021, id. 101227.

[8] Ali, M., M. Shahzad, F. Sultan, and W. A. Khan. Numerical analysis of chemical reaction and non-linear radiation for magneto-Cross nanofluid over a stretching cylinder. *Applied Nanoscience*, Vol. 10, 2020, pp. 3259–3267.

[9] Salahuddin, T., A. Maqsood, M. Awais, M. Khan, and M. Altanji. Significance of MHD Cross nanofluid analysis near a stretched surface with double stratification and activation energy. *International Communications in Heat and Mass Transfer*, Vol. 143, 2023, id. 106732.

[10] Shi, Q. H., A. Hamid, M. I. Khan, R. N. Kumar, R. J. P. Gowda, B. C. Prasannakumara, et al. Numerical study of bio-convection flow of magneto-Cross nanofluid containing gyrotactic microorganisms with activation energy. *Scientific Reports*, Vol. 11, 2021, id. 16030.

[11] Shoaib, M., K. S. Nisar, M. A. Z. Raja, R. Tabassum, and Z. Sabir. A stagnation point flow of Cross nanofluid flow: Levenberg Marquardt backpropagation computational approach. *Zeitschrift fuer Angewandte Mathematik und Mechanik*, Vol. 104, 2024, id. e202300236.

[12] Aziz, A., W. A. Khan, and I. Pop. Free convection boundary layer flow past a horizontal flat plate embedded in porous medium filled by nanofluid containing gyrotactic microorganisms. *International Journal of Thermal Sciences*, Vol. 56, 2012, pp. 48–57.

[13] Tham, L., R. Nazar, and I. Pop. Mixed convection flow over a solid sphere embedded in a porous medium filled by a nanofluid containing gyrotactic microorganisms. *International Journal of Heat and Mass Transfer*, Vol. 62, 2013, pp. 647–660.

[14] Ibrahim, M. Numerical analysis of time-dependent flow of viscous fluid due to a stretchable rotating disk with heat and mass transfer. *Results in Physics*, Vol. 18, 2020, id. 103242.

[15] Chu, Y. M., S. Aziz, M. I. Khan, S. U. Khan, M. Nazeer, I. Ahmad, et al. radiative bioconvection flow of Maxwell nanofluid configured by bidirectional oscillatory moving surface with heat generation phenomenon. *Physica Scripta*, Vol. 95, No. 10, 2020, id. 105007.

[16] Islam, S., M. Jawad, A. Saeed, Z. Shah, M. Zubair, A. Khan, et al. MHD Darcy-Forchheimer flow due to gyrotactic microorganisms of

Casson nanoparticles over a stretched surface with convective boundary conditions. *Physica Scripta*, Vol. 96, 2021, id. 015206.
[17] Khan, N. S., Q. Shah, and A. Sohail. Dynamics with Cattaneo-Christov heat and mass flux theory of bioconvection Oldroyd-B nanofluid. *Advances in Mechanical Engineering*, Vol. 12, No. 8, 2020, pp. 1–20.
[18] Nadeem, S., A. Amin, and N. Abbas. On the stagnation point flow of nanomaterial with base viscoelastic micropolar fluid over a stretching surface. *Alexandria Engineering Journal*, Vol. 59, 2020, pp. 1751–1760.
[19] Ferdows, M., A. Hossan, M. Z. I. Bangalee, S. Sun, and F. Alzahrani. Stability theory of nano-fluid over an exponentially stretching cylindrical surface containing microorganisms. *Scientific Reports*, Vol. 10, No. 1, 2020, pp. 1–18.
[20] Sajid, T., M. Sagheer, S. Hussain, and F. Shahzad. Impact of double-diffusive convection and motile gyrotactic microorganisms on magnetohydrodynamics bioconvection tangent hyperbolic nanofluid. *Open Physics*, Vol. 18, No. 1, 2020, pp. 74–88.
[21] Usman, M. I., F. Khan, S. U. Shah, A. Khan, and Y.-M. Ghaffari. Chu Heat and mass transfer analysis for bioconvective flow of Eyring Powell nanofluid over a Riga surface with nonlinear thermal features. *Numerical Methods for Partial Differential Equations*, Vol. 38, 2022, pp. 777–793.
[22] Hussain, S., F. Haq, H. A. Ghazwani, M. Saleem, and A. Hussain. Entropy optimization in bio-convective chemically reactive flow of micropolar nanomaterial with activation energy and gyrotactic microorganisms. *Case Studies in Thermal Engineering*, Vol. 55, 2024, id. 104131.
[23] Olkha, A. and R. Choudhary. Investigation of melting heat transfer in viscous nanofluid flow including micro-organisms and entropy generation due to an inclined exponentially stretching sheet. *Journal of Nanofluids*, Vol. 13, 2024, pp. 446–463.
[24] Ali, A., S. Sarkar, and S. Das. Bioconvective chemically reactive entropy optimized Cross-nano-material conveying oxytactic microorganisms over a flexible cylinder with Lorentz force and Arrhenius kinetics. *Mathematics and Computers in Simulation*, Vol. 205, 2023, pp. 1029–1051.
[25] Bilal, S., K. Pan, Z. Hussain, B. Kada, A. A. Pasha, and W. A. Khan. Darcy-Forchheimer chemically reactive bidirectional flow of nanofluid with magneto-bioconvection and Cattaneo-Christov properties. *Tribology International*, Vol. 193, 2024, id. 109313.
[26] Choi, S. U. and J. A. Eastman. *Enhancing thermal conductivity of fluids with nanoparticles (No. ANL/MSD/CP-84938; CONF-951135-29)*, Argonne National Lab., IL, United States, 1995.
[27] Ellahi, R., S. U. Rahman, S. Nadeem, and N. S. Akbar. Blood flow of nanofluid through an artery with composite stenosis and permeable walls. *Applied Nanoscience*, Vol. 4, No. 8, 2014, pp. 919–926.
[28] Rashidi, M. M., M. M. Bhatti, M. A. Abbas, and M. E. S. Ali. Entropy generation on MHD blood flow of nanofluid due to peristaltic waves. *Entropy*, Vol. 18, No. 4, 2016, id. 117.
[29] Chahregh, H. S. and S. Dinarvand. TiO_2-Ag/blood hybrid nanofluid flow through an artery with applications of drug delivery and blood circulation in the respiratory system. *International Journal of Numerical Methods for Heat & Fluid Flow*, Vol. 30, No. 11, 2020, pp. 4775–4796.
[30] Manjunatha, S., R. Saadeh, B. A. Kuttan, T. N. Tanuja, A. Zaib, U. Khan, et al. Influence of non-linear thermal radiation on the dynamics of homogeneous and heterogeneous chemical reactions between the cone and the disk. *High Temperature Materials and Processes*, Vol. 43, No. 1, 2024, id. 20240052.
[31] Sheikholeslami, M. Numerical approach for MHD Al_2O_3-water nanofluid transportation inside a permeable medium using innovative computer method. *Computer Methods in Applied Mechanics and Engineering*, Vol. 344, 2019, pp. 306–318.
[32] Ayub, A., Z. Sabir, H. A. Wahab, M. Balubaid, S. R. Mahmoud, M. R. Ali, et al. Analysis of the nanoscale heat transport and Lorentz force based on the time-dependent Cross nanofluid. *Engineering with Computers*, Vol. 39, 2023, pp. 2089–2108.
[33] Ramesh, G. K., R. Saadeh, J. K. Madhukesh, A. Qazza, U. Khan, A. Zaib, et al. Neural network algorithms of a curved riga sensor in a ternary hybrid nanofluid with chemical reaction and Arrhenius kinetics. *Journal of Radiation Research and Applied Sciences*, Vol. 17, No. 4, 2024, id. 101078.
[34] Alharbi, L. F., R. Saadeh, A. Ishak, U. Khan, S. M. Hussain, J. K. Madhukesh, et al. Heat transfer characteristics in a non-Newtonian (Williamson) hybrid nanofluid with Hall and convective boundary effects. *High Temperature Materials and Processes*, Vol. 43, No. 1, 2024, id. 20240056.
[35] Vinothkumar, B., R. Saadeh, T. Poornima, A. Qazza, P. Sreenivasulu, A. S. Rao, et al. Two-phase numerical simulation of thermal and solutal transport exploration of a non-Newtonian nanomaterial flow past a stretching surface with chemical reaction. *Open Physics*, Vol. 22, No. 1, 2024, id. 20240036.
[36] Tanuja, T. N., S. Manjunatha, H. S. Migdadi, R. Saadeh, A. Qazza, U. Khan, et al. Leveraging artificial neural networks approach for thermal conductivity evaluation in porous rectangular wetted fins filled with ternary hybrid nanofluid. *Journal of Radiation Research and Applied Sciences*, Vol. 17, No. 4, 2024, id. 101125.
[37] Bejan, A. *Entropy generation minimization*, CRC Press, New York, NY, USA, 1996.
[38] Bejan, A. and J. Kestin. Entropy generation through heat and fluid flow. *Journal of Applied Mechanics*, Vol. 50, 1983, id. 475.
[39] Qing, J., M. M. Bhatti, M. A. Abbas, M. M. Rashidi, and M. S. Ali. Entropy generation on MHD Casson Nanofluid flow over a porous stretching/shrinking surface. *Entropy*, Vol. 18, 2016, id. 123.
[40] Sithole, H., H. Mondal, and P. Sibanda. Entropy generation in a second grade magnetohydrodynamics nanofluid flow over a convectively heated stretching sheet with nonlinear thermal radiation and viscous dissipation. *Results in Physics*, Vol. 9, 2018, pp. 1077–1085.
[41] Shit, G. C. and S. Mukherjee. MHD graphene-polydimethylsiloxane Maxwell nanofluid flow in a squeezing channel with thermal radiation effects. *Applied Mathematics and Mechanics*, Vol. 40, 2019, pp. 1269–1284.
[42] Abbas, S. Z., W. A. Khan, H. Sun, M. Ali, M. Irfan, M. Shahzed, et al. Mathematical modeling and analysis of Cross nanofluid flow subjected to entropy generation. *Applied Nanoscience*, Vol. 10, 2020, pp. 3149–3160.
[43] Siddiqui, B. K., S. Batool, and Q. M. U. Hassan. Repercussions of homogeneous and heterogeneous reactions of 3D flow of Cu-water and Al_2O_3-water nanofluid and entropy generation estimation along stretching cylinder. *Ain Shams Engineering Journal*, Vol. 13, No. 1, 2022, id. 101493.
[44] Tlili1, I., M. Khan, T. Salahuddin, A. Tanveer, and A. Hussain. Entropy generation minimization and chemical response for Williamson fluid flow with thermal diffusion. *Applied Nanoscience*, Vol. 10, 2020, pp. 3123–3131.
[45] Shafiq, A., A. B. Colak, T. N. Sindhu, S. A. Lone, and T. A. Abushal. Modeling and survival exploration of breast carcinoma: a statistical, maximum likelihood estimation, and artificial neural

network perspective. *Artificial Intelligence Life Sci*, Vol. 4, 2023, id. 100082.

[46] Akbar, N. S., T. Zamir, T. Noor, T. Muhammad, and M. R. Ali. Heat transfer enhancement using ternary hybrid nanofluid for Cross-viscosity model with intelligent Levenberg-Marquardt neural networks approach incorporating entropy generation. *Case Studies in Thermal Engineering*, Vol. 63, 2024, id. 105290.

[47] Chandra, P. and R. Das. A hybrid machine learning algorithm for studying magnetized nanofluid flow containing gyrotactic microorganisms via a vertically inclined stretching surface. *International Journal for Numerical Methods in Biomedical Engineering*, Vol. 40, No. 1, 2024, id. e3780.

[48] Akbar, N. S., T. Zamir, J. Akram, T. Noor, and T. Muhammad. Simulation of hybrid boiling nano fluid flow with convective boundary conditions through a porous stretching sheet through Levenberg Marquardt artificial neural networks approach. *International Journal of Heat and Mass Transfer*, Vol. 228, 2024, id. 125615.

[49] Shah, F. A., N. S. Akbar, T. Zamir, M. A. El-Rahman, and W. A. Khan. Thermal energy analysis using artificial neural network and particle swarm optimization approach in partially ionized hyperbolic tangent material with ternary hybrid nanomaterials. *Swarm and Evolutionary Computation*, Vol. 91, 2024, id. 101775.

[50] Alghamdi, M., N. S. Akbar, T. Zamir, and T. Muhammad. Double layered combined convective heated flow of Eyring-Powell fluid across an elevated stretched cylinder using intelligent computing approach. *Case Studies in Thermal Engineering*, Vol. 54, 2024, id. 104009.

[51] Srinivasacharya, D. and R. S. Kumar. Neural network analysis for bioconvection flow of Casson fluid over a vertically extending sheet. *International Journal of Applied and Computational Mathematics*, Vol. 9, 2023, id. 80.

[52] Alghamdi, M., T. Zamir, N. S. Akbar, and T. Muhammad. Neural intellectual computing systems for the analysis of thermally stratified mixed convective micropolar liquid with the interaction of thermal diffusive nanofluid over a heated sheet. *Neural Computing and Applications*, Vol. 37, 2024, pp. 1575–1599.

[53] Shankaralingappa, B. M., B. J. Gireesha, B. C. Prasannakumara, and B. Nagaraja. Darcy-Forchheimer flow of dusty tangent hyperbolic fluid over a stretching sheet with Cattaneo-Christov heat flux. *Waves Rand Complex Media*, Vol. 33, No. 3, 2023, pp. 742–761.

[54] Ali, F., A. Zaib, S. A. Lone, Z. Raizah, A. Saeed, and H. Yasmin. Thermal radiative on bio-convection flow with stefan blowing effects over a rotating disk in a porous medium. *Journal of Thermal Analysis and Calorimetry*, Vol. 150, 2024, pp. 2683–2701.

Appendix

```
>>P=[1:2247,1:6]; %input
>>T=[1:2247,7:8]; %target
>>a=[2188:2247,1:6]; %test input
>>s=[2188:2247,7:8]; %test target
>>[pn1,PS] = mapminmax(P);
>>[tn1,TS] = mapminmax(T);
>>[an1,AS] = mapminmax(a);
>>[sn1,SS] = mapminmax(s);
>>[pn1,tn1] = simplefit_dataset;
>>[an1,sn1] = simplefit_dataset;
>>net = feedforwardnet([8 4]);
>>[net,TR]=train(net,pn1,tn1)
>>y2=sim(net,an1);
>>y2_again = mapminmax('reverse',y2',TS);
>>plot(y2_again,'r')
>>hold
>>plot(s)
>>d = (y2_again-s).^2
>>mse1 = mean(d)
```